Towards a realistic simulation of boreal summer tropical rainfall climatology in state-of-the-art coupled models: Role of the background snow-free land albedo

P. Terray[1,2,*], K.P. Sooraj[3], S. Masson[2], R.P.M. Krishna[4], G. Samson[5], A.G. Prajeesh[3]

[1] *Indo-French Cell for Water Sciences, IISc-NIO-IITM–IRD Joint International Laboratory, IITM, Pune, India*

[2] *Sorbonne Universites (UPMC, Univ Paris 06)-CNRS-IRD-MNHN, LOCEAN Laboratory, 4 place Jussieu, F-75005 Paris, France*

[3] *Centre for Climate Change Research, Indian Institute of Tropical Meteorology, Pune, India*

[4] *Indian Institute of Tropical Meteorology, Pune, India*

[5] *Mercator Océan, Ramonville-Saint-Agne, France*

Revised for *Climate Dynamics,* 14th July 2017

Corresponding author address: Pascal Terray, Indian Institute of Tropical Meteorology, Pune 411008, India. E-mail: terray@locean-ipsl.upmc.fr

Abstract

State-of-the-art global coupled models used in seasonal prediction systems and climate projections still have important deficiencies in representing the boreal summer tropical rainfall climatology. These errors include prominently a severe dry bias over all the Northern Hemisphere monsoon regions, excessive rainfall over the ocean and an unrealistic double Inter-Tropical Convergence Zone (ITCZ) structure in the tropical Pacific. While these systematic errors can be partly reduced by increasing the horizontal atmospheric resolution of the models, they also illustrate our incomplete understanding of the key mechanisms controlling the position of the ITCZ during boreal summer.

Using a large collection of coupled models and dedicated coupled experiments, we show that these tropical rainfall errors are partly associated with insufficient surface thermal forcing and incorrect representation of the surface albedo over the Northern Hemisphere continents. Improving the parameterization of the land albedo in two global coupled models leads to a large reduction of these systematic errors and further demonstrates that the Northern Hemisphere subtropical deserts play a seminal role in these improvements through a heat low mechanism.

Keywords: tropical rainfall climatology, monsoons, global coupled models, surface albedo, heat low, deserts

1. Introduction

The monsoon systems across the Northern Hemisphere (NH) can be interpreted as the seasonal swings over land of the large-scale Inter-Tropical Convergence Zone (ITCZ) cells due to the intense solar heating of the northern continents during boreal summer (Schneider et al. 2014). The monsoon rainfall in these complex land-atmosphere-ocean systems provides fresh-water for people who live in Africa, America, South and East Asia and the fate of these monsoons in a global warming environment is of great concern for about one-half of the world population (IPCC 2013).

Yet, despite decades of intensive research to address these issues, which have important socio-economic implications, almost all climate and weather prediction Coupled General Circulation Models (CGCMs) still fail in capturing correctly even the basic characteristics of the boreal summer monsoon systems such as their precipitation pattern and amplitude (Richter et al. 2012; Roehrig et al. 2013; Sperber et al. 2013; Prodhomme et al. 2014, 2016). The multi-model mean from CGCMs participating in phase 5 of the Coupled Model Inter-comparison Project (Taylor et al. 2012; CMIP5) is, for example, affected by a severe dry bias over South and East Asia, central America and West Africa and an opposite wet bias over the adjacent oceans, reflecting a too equatorward simulated position of the ITCZ during boreal summer (Fig. 1a). The CMIP models also exhibit a double ITCZ problem over the tropical Pacific (Fig. 1a; Lin 2007; Reichler and Kim 2008). These tropical rainfall biases are well above the rainfall standard deviation computed across the CMIP5 models in most oceanic and land regions (see the contours in Fig. 1a) attesting the robustness of these errors. The only exception is the land areas where orography is important, such as the foothills of the Himalayas. Thus, the amplitude of the dry bias, especially in these orographic regions, is also partly dependent on the horizontal resolution of the CMIP5 models (Johnson et al. 2016).

Furthermore, climate projections performed by the CMIP models are highly uncertain and even disagree for the sign of the rainfall anomalies over the Sahel region (Roehrig et al. 2013; Biasutti 2013). Over South Asia, most of the CGCMs project increasing precipitation in a future warming scenario, but decreasing large-scale circulation and thermodynamic drivers of the monsoon (Sooraj et al. 2015; Sabeerali et al. 2015). Thus, it has become a common belief that these rainfall projections are unreliable because current CGCMs have not reached yet a sufficient degree of maturity as far as the West African and Indian monsoons are concerned

(Roehrig et al. 2013; Sabeerali et al. 2015; Annamalai et al. 2015).

The Climate Forecast System version 2 (CFS; Saha et al. 2014), which is the current operational climate prediction model for seasonal prediction in the US (at the National Centers for Environmental Prediction, NCEP) and in India (as part of the Monsoon Mission program see url: http://www.tropmet.res.in/monsoon/), and the SINTEX-F2 CGCM (SINTEX; Masson et al. 2012), which is also a standard tool to forecast and simulate tropical variability (Doi et al. 2016) share exactly the same rainfall biases (Figs. 1b and c) despite of having a higher horizontal resolution than most CMIP5 models (see Section 2). Consequently, these rainfall errors do not only concern climate models, but also seasonal dynamical forecasting systems, thus adversely affecting the monsoon dynamical prediction skill (Kim et al. 2013).

While increasing horizontal atmospheric resolution may help to reduce these biases (Prodhomme et al. 2016), these recurrent problems of state-of-the-art CGCMs reflect also our lack of understanding of the physical processes regulating the boreal summer monsoon rainfall characteristics (Annamalai et al. 2015; Hourdin et al. 2015; Johnson et al. 2016). So far, these rainfall biases have been attributed to regional Sea Surface Temperature (SST) errors (Roehrig et al. 2013; Richter 2015; Bollasina and Ming 2013; Levine et al. 2013) and deficiencies in the representation of sub-grid scale processes, especially convection and cloud parameterization schemes in too coarse atmospheric models (Sabeerali et al. 2015; Dai 2006; Stephens et al. 2010). In contrast, the role of land surface processes in the dry monsoon bias has received less attention, despite pioneering investigations have suggested that these processes have a significant influence on large-scale circulation over arid regions and the monsoons (Charney et al. 1977; Sud and Smith 1985). Subsequently, many studies have addressed the question of land, orography and Earth's continental configuration forcing on the monsoons, but not in the perspective of reducing model biases (Dirmeyer 1998; Chakraborty 2002; Liang et al. 2005a; Boos and Kuang 2010; Wu et al. 2012 among many others). Recently, there are a few regional studies suggesting that improving the representation of land surface processes in CGCMs or regional models may offer a way of advancing their performance and skill for the NH monsoons (Alessandri et al. 2007; Richter et al. 2012; Kelly and Mapes 2010; Boos and Hurley 2013; Samson et al. 2016; Ashfaq et al. 2016).

Here, we demonstrate that land surface albedo and temperature errors play a significant and global role in the spurious southward ITCZ position over the monsoon regions during boreal summer in current CGCMs. Our work raises the possibility that important errors in land surface parameterization may explain a large part of the systematic tropical rainfall errors in state-of-the-art CGCMs.

The article is organized as follows. In section 2, we give a brief overview of the datasets, the collection of CMIP5 models and the two CGCMs used in our dedicated sensitivity coupled experiments. Section 3 is devoted to an analysis of rainfall, Sea Level Pressure (SLP), surface temperature, albedo and radiation biases during boreal summer in state-of-the-art CGCMs suggesting that tropical rainfall errors in current CGCMs are partly associated with insufficient surface thermal forcing and incorrect representation of the surface albedo over the NH continents. Section 4 focuses more specifically on the role of the surface land albedo and skin temperature biases on the rainfall and atmospheric circulation biases during boreal summer with the help of dedicated experiments with two state-of-the-art CGCMs. Conclusions and prospects for future work are given in section 5.

2. Datasets, climate models and sensitivity coupled experiments

Almost all our analysis and diagnostics pertain to the boreal summer season (June to September, JJAS).

2.a Satellite-based and reanalysis datasets

To compare model outputs with observations, we make use of three observational datasets: 1) monthly-accumulated precipitation from the Global Precipitation Climatology Project (GPCP version 2.1; Huffman et al. 2008) over the 1979-2010 period; 2) monthly-mean atmospheric variables (e.g. surface temperature, wind, SLP and sensible heat flux) derived from the 0.75° ERA-Interim reanalysis, the latest global atmospheric reanalysis produced by the European Centre for Medium-Range Weather Forecasts (Dee et al. 2011; data available at url: http://apps.ecmwf.int/datasets/data/interim-full-daily), over the 1979-2014 period, and, finally, 3) monthly-mean surface and Top-Of-the-Atmosphere (TOA) radiative fluxes computed from the Clouds and Earth's Radiant Energy System (CERES; Energy Balance and Filled (EBAF) top-of-the atmosphere and surface fluxes version 2.8; Kato et al. 2013) obtained from the NASA Langley Research Center over the 2000-2014 period from url: http://ceres.larc.nasa.gov/products.php?product=EBAF-Surface.

Since there are uncertainties in the observations, especially for rainfall, we have also cross-validated our analyses with the Climate Prediction Center (CPC) Merged Analysis of Precipitation (CMAP; Xie and Arkin 1997). Despite of the fact that CMAP produces higher tropical rainfall over the ocean than GPCP due to the use of atoll data in CMAP (Yin et al. 2004), the results are very similar if we use CMAP as a reference in our analyses (not shown), demonstrating that the CGCM rainfall biases, which we are discussing here are much higher than the uncertainties in the rainfall observations. However, since GPCP is believed to be much more reliable than CMAP for tropical rainfall (Yin et al. 2004), we only show the results using GPGP in this study.

The CERES-EBAF data are commonly used for model output evaluation, since they include albedo estimates for both land and ocean, and are produced by deriving the energy balance from Aqua, Terra and geostationary satellites, and adjusting it to that inferred from the measured warming of the oceans (Loeb et al. 2012; Kato et al. 2013). A complete description of the data is available in the CERES website (url: http://ceres.larc.nasa.gov).

For our numerical experiments with updated snow-free background diffuse albedo over land (described in section 2.b), we make use of the Moderate Resolution Imaging Spectro-radiometer (MODIS) snow-free gap-filled white-sky (diffuse) albedo product MCD43GF-v5 (Schaaf et al. 2011) for three different spectral bands: total short-wave (SW, 0.3–5.0 μm), visible (VIS, 0.3–0.7 μm), and near-infrared (NIR, 0.7–5.0 μm). This product is generated by merging data from the Terra and Aqua platforms produced every 8 days, with 16-days acquisition and available on a 0.05° global grid for land surface only. Like any algorithm to derive surface broadband albedo from polar-orbit satellite observations, MODIS used three steps to estimate surface albedo: atmospheric correction, Bidirectional Reflectance Distribution Function (BRDF) angular modeling and narrow-to-broadband conversions. Since MODIS is based on BRDF modeling specifically developed for land surface, MODIS albedo datasets do not include background surface albedo for the ocean, excepted for few points where ocean depth is relatively small (Schaaf et al. 2011). Moreover, it is important to note that some regions are systematically masked by clouds, which makes direct albedo measurements difficult, or even impossible. A temporal interpolation has been applied to fill these missing values. The MODIS snow-free climatology for the three different bands is computed over the 2003-2013 period. The accuracy of this product is about 2% when compared to ground observations. More details about satellites, data processing and quality controls of the MODIS data can be found in Schaaf et al. (2011).

2.b Coupled models and numerical experiments

In order to assess precipitation, temperature and albedo biases of current CGCMs, we first used the monthly mean output from CMIP5 models (Taylor et al. 2012) available at url: http://cmip-pcmdi.llnl.gov/cmip5/data_portal.html. We analyze the twentieth century simulations of 36 CMIP5 models (Table 1) and for all the models we use the first ensemble member (‘‘r1i1p1’’ from CMIP5 database) for each model. The albedo is calculated as the ratio between the upward and downward shortwave radiations at the surface as obtained from CMIP5 model outputs. The 20-year mean during 1980-1999 in these historical simulations defines the present-day climatology for CMIP5 models.

For our numerical sensitivity experiments, we used two state-of-the-art CGCMs, the SINTEX_F2 and CFSv2 coupled models (SINTEX and CFS hereafter). A comprehensive description of SINTEX can be found in Masson et al. (2012). Its main components relevant for our study are summarized as follows. The atmosphere model is ECHAM5.3 and is run at T106 spectral resolution (about 1.125° by 1.125°) with 31 hybrid sigma-pressure levels (Roeckner et al. 2003). The oceanic component has a horizontal resolution of ~0.5°, 31 unevenly spaced vertical levels and includes an ice model. Atmosphere and ocean are coupled, without any flux corrections, every 2 h. The second coupled model used here is the Climate Forecast System version 2 (CFS) developed by the National Centers for Environmental Prediction (NCEP) and used currently for seasonal forecasting in the US and India (Saha et al. 2014). Its atmospheric model, the Global Forecast System (GFS) is run at T126 spectral resolution (about 0.9° by 0.9°) with 64 sigma-pressure hybrid levels. Its oceanic component has a 0.25–0.5° horizontal resolution, 40 vertical levels and includes an ice model. The atmosphere and ocean exchange quantities such as heat and momentum fluxes every half an hour, with no flux adjustment or correction. See Saha et al. (2014) for further details on the CFS model and its components.

Snow free albedo parameterization in CGCMs is based on the assumption that surface albedo is primarily an intrinsic property of surface characteristics, depending also (for some models, but not all) on the angular and spectral distributions of the incident solar radiation, but that its dependence on atmospheric conditions has a relatively minor effect.

The land surface scheme in ECHAM5.3 (the atmospheric component of SINTEX) uses a background white-sky (e.g. diffuse) SW albedo without any seasonal or diurnal cycle over snow-free land surfaces (Roeckner et al. 2003). These albedos are prescribed from fixed tabulated values depending only on a land cover classification. This classification contains 74 land use classes and for each class mean values for background surface albedo, fractional vegetation cover and other vegetation properties are provided. This information is subsequently aggregated to the model grid scale by averaging the vegetation parameters of all land cover types, which are located in one model grid cell for the chosen resolution. Thus, the albedo over snow-free land surfaces in ECHAM5.3 may be considered as a fixed boundary land condition and stays constant for each grid-point at each time step of the simulation.

Finally, the surface albedo of a model grid box is derived as the area weighted linear average of the background albedo over the fraction with snow-free land, the albedo over the water fraction and the albedo over snow-covered grid area. A more comprehensive description of the ECHAM5.3 albedo parameterization can be found in Roeckner et al. (2003). This scheme was intended for broadband solar flux and made no differentiation between direct and diffuse fluxes (beams) or spectral bands, which is a strong limitation of the ECHAM5.3 model.

The albedo parameterization in the GFS (the atmospheric component of CFS) takes into account that the albedos for direct-beam and diffuse fluxes have different characteristics, especially that the direct albedo does depend on the Solar Zenith Angle (SZA) and thus do vary during the day (Hou et al. 2002). Furthermore, the diffuse albedo is prescribed differently for the ultraviolet and visible band (VIS, <0.7 **μ**m) and the near-infrared band (NIR, >0.7 **μ**m) and its seasonal variations, as well as its "strong" or "weak" dependency to the SZA, are also taken into account in addition to its spatial variations associated with the different vegetation types (Hou et al. 2002). The direct beam albedo, which strongly depends on the SZA, is then parameterized from the prescribed diffuse albedo for each spectral band (e.g. VIS and NIR) using a scheme described by Hou et al. (2002). Although vegetation is not explicitly represented in the GFS scheme, it can be regarded as implicitly resolved by the prescribed diffuse surface albedos, which vary in space and time according to the soil and vegetation types. Finally, as in ECHAM5.3, GFS separately computes at each time step albedos for soil, snow, and vegetation, and then estimates the total albedo of a grid box as an average of these albedos weighted by the representative area fractions.

Both in GFS and ECHAM5.3, the prescribed land surface snow-free diffuse albedo are estimated off-line and "manually" from isolated field measurements and old (more than 30 years for GFS) and outdated classifications of vegetation. These aspects of the two models have not been modified for a long time by the developers of GFS and ECHAM. Before the era of new satellite products like MODIS (Schaaf et al. 2011), getting the correct values for this kind of land surface snow-free albedo was very difficult as we will demonstrate in the next section.

The type of albedo parameterization we have described above is typical of seasonal forecasting and "simple" coupled models currently in use. This differs from Earth System Models (ESMs) and many CMIP5 models in which the surface snow-free diffuse and direct albedos are usually parameterized from a vegetation and soil classification (eventually evolving dynamically in time) through a table (or a land model) giving the correspondences between soil and vegetation categories (e.g. Plant Functional Types or biomes) and background surface snow-free albedo values (Houldcroft et al. 2009). In many cases, the snow-free land albedo for each biome is explicitly computed as a function of foliage density and of a minimum prescribed albedo, which corresponds to the maximum of foliage density for this biome. In each continental box, a fixed (or dynamical) mosaic of prescribed biomes can coexist and the snow-free albedo of that box can be estimated by a surface-weighted average of the albedos of the coexisting biomes (Houldcroft et al. 2009; Vamborg et al. 2014).

Finally, note that the standard output from most global climate models includes monthly averaged reflected and incoming total SW radiation fluxes at surface and their ratio is defined as the monthly averaged albedo. This would be consistent with the albedo computed from the CERES-EBAF dataset described above and may differ from the background snow-free diffuse albedo from MODIS and prescribed in the models.

We first run 210-years and 80-years control experiments (named SINTEX and CFS, respectively) with the standard configuration of SINTEX and CFS, respectively. These reference simulations are then compared with several sensitivity experiments for each coupled model. Table 2 summarizes all the model simulations used in this study.

To examine first the role of land albedo on the monsoon dry biases, sensitivity experiments were performed by setting to zero everywhere the snow-free background land albedo in the two models (ZERO_SINTEX and ZERO_CFS, respectively). ZERO_SINTEX and ZERO_CFS have been time integrated over a period of 60 and 30 years, respectively.

To evaluate the impact of the errors associated with prescribed tabulated albedo values in ECHAM5.3, we have replaced these annual background albedos by a weekly climatology of white-sky (e.g. diffuse) albedo for total SW broadband from the MODIS MCD43GF-v5 product. A seasonal cycle of the background broadband SW albedo has also been incorporated since previous works have demonstrated the significance of this seasonal cycle (Liang et al. 2005b; Yang et al. 2008). Similarly, the seasonally prescribed tabulated diffuse albedo values for the VIS and NIR bands in GFS (four seasons are used) have been replaced by corresponding estimates from MODIS MCD43GF-v5 product. In GFS, the snow-free diffuse albedo values are changed daily by linear interpolation from these prescribed mean seasonal climatological data and these aspects have not been modified. The sensitivity of the simulated climate to these new background albedo parameterizations implemented in the models is assessed with the help of two climate simulations of 110 years for MODIS_SINTEX and 60 years for MODIS_CFS.

Finally, two simulations were performed using again a land background diffuse albedo from MODIS MCD43GF-v5 product and where, in addition the land background diffuse albedo has been further decreased by -0.2 over the Sahara, Arabia and Middle-East deserts (domain: latitude 15°-40°N, longitude 20°W-75°E). These two simulations DESERT_SINTEX and DESERT_CFS have been time integrated for a period of 60 and 30 years, respectively.

It is important to highlight that the MODIS configuration implemented in our two coupled models really represents an upgrade of these CGCMs as we will demonstrate in the following sections. On the other hand, the ZERO and DESERT experiments described above must be considered as idealized experiments useful for illustrating, respectively, the potential maximum effect and the main mechanisms associated with the changes of the background snow-free albedo.

All the sensitivity experiments are initialized exactly as their respective control runs. For SINTEX, the initial atmospheric conditions are taken as January climatologies computed from ERA15 reanalysis (this is the standard initialization procedure of the ECHAM model, the atmospheric component of SINTEX, as given by the developers of this model) and the ocean starts from rest, initialized by a mean Levitus T–S field. For the land, the standard initialization and prescribed climatology files (for parameters like soil wetness, snow depth, surface roughness length, field capacity of soil, vegetation and soil types, leaf area index, vegetation ratio) of the ECHAM model have also been used. For the CFS, all the experiments are coupled free-runs initialized from initial conditions of 31 July 2014 taken from the CFSv2 Operational Analysis or Climate Data Assimilation System (CDAS) developed at NCEP (see url:https://data.noaa.gov/dataset/climate-forecast-system-version-2-cfsv2-operational-analysis). Also both models employ fixed CO_2 concentrations corresponding to present-day conditions.

The surface temperature drift and TOA imbalance in the two models can be summarized as follow. SINTEX has only a small positive TOA energy imbalance (0.17 W/m^2), which is fairly constant during the control simulation and, consistently, a very small positive temperature drift (about 0.3-0.4°C for the surface mean global temperature for the 210 years). MODIS_SINTEX exhibits a similar global temperature evolution, with a constant temperature offset, during its whole integration. On the other hand, DESERT_SINTEX and ZERO_SINTEX exhibit a rapid warming drift at the beginning of the integrations (about 10 years) and are going progressively in a small positive temperature drift after. This behavior is consistent with the facts that the SINTEX model is a "well-tuned" climate model and that it adjusts progressively to the increased absorbed solar radiation by the land surface all year round. Note, however, that the deep ocean may take several hundred of years to reach equilibrium meaning that the DESERT_SINTEX and ZERO_SINTEX experiments, especially ZERO_SINTEX, are transient runs.

On the other hand, the CFS control run has a fairly constant TOA energy imbalance of about 5.4 W/m^2 and is affected by a negative surface temperature drift during the first 10-20 years of simulation and is stabilized hereafter. These two features are well known problems in the CFSv2 model (see Swapna et al. 2015; for further details) and suggest that some sources of energy are not tracked correctly in CFSv2. Interestingly, the initial negative temperature drift is partly or fully corrected in the MODIS_CFS, DESERT_CFS and ZERO_CFS experiments, so these experiments are more stable than the control run (not shown). This suggests that the large land surface albedo bias is an important contributor to the cold surface temperature bias in CFSv2 (see also Rai and Saha 2017). Since CFS is affected by an important TOA radiative imbalance, it cannot be considered as a climate model even though CMIP simulations have also been performed with CFS (Saha et al. 2014). However, our investigation does not focus only on biases of CMIP5 or climate models, but also on biases in seasonal forecasting coupled models currently in use and the CFS is probably one of the best examples in this category, which justifies its use here. CFS coupled free-runs, as done here, have been performed in many studies and are especially useful to diagnose model's errors in the US and India forecasting systems based on the CFS (Goswami et al. 2014; Swapna et al. 2015; Rai and Saha 2017 among many others).

The differences between the sensitivity and control experiments for each model are taken as the model response to the change of the background snow-free land albedo. For the SINTEX experiments, all the analyses presented in the following sections exclude the first 10 years of the simulations to let the coupled simulations spin-up. For the CFS model, which is a seasonal forecasting coupled model, data from the first 5 years of each simulation are disregarded from the analyses. However, in both cases, results are robust and do not depend on if more data is excluded from the start of the simulations (not shown).

A local statistical test is applied to the various differences fields in order to assess the statistical significance of the results and to take into account the intrinsic internal variability of the models. More precisely, the statistical significance of the differences was estimated through the procedure in Noreen (1989), based on a permutation test with 9999 shuffles, and differences significant at the 95% confidence level are indicated in the figures. More details about this statistical test are given in Terray et al. (2003). The robustness of the responses is also attested by the similarity of the results between the two models rather than by standard statistical significance, which can be physically misleading.

3. Rainfall, temperature, SLP and albedo biases in state-of-the-art coupled models.

Our main investigation is based on two state-of-the-art global CGCMs (CFS and SINTEX, see section 2 for details), which allow a full interplay between ocean dynamics, land processes, radiation, atmospheric convection and geography of the continents. As pointed out in the introduction, the boreal summer rainfall climatology of these two models is very similar with those of the CMIP5 CGCMs and exhibits the same systematic errors (Figs. 1b and c). These two CGCMs also exhibit systematic errors similar to CMIP5 models in simulating global SSTs and SLPs during boreal summer (Fig. 2, SLP in contours). As an illustration, all the models display a cold tongue bias over the equatorial Pacific (Reichler and Kim 2008) and a strong overestimation of SST over the eastern tropical Pacific and Atlantic oceans (Hourdin et al. 2015; Richter 2015). Numerous studies have suggested that these SST errors are important for explaining the misrepresentation of the monsoons or the Pacific ITCZ in current CGCMs (Roehrig et al. 2013; Prodhomme et al. 2014; Lin 2007; Reichler and Kim 2008; Bollasina et Ming 2013; Levine et al. 2013; Dai 2006; Wang et al. 2014; Sandeep and Ajayamohan 2014), but without providing a way forward to correct these SST errors in current CGCMs.

Interestingly, surface temperature biases over the NH continents are much larger than SST biases over the adjacent oceans and exhibit some consistency across CGCMs (Fig. 2). Specifically, there are large cold biases associated with positive SLP errors over the Sahara, Arabia and Middle-East deserts and mid-to-high latitudes of Asia, while warm biases prevail over South Asia, Sahel and Amazon Basin consistent with the deficient boreal summer monsoon rainfall over these regions. In order to understand the origins of these consistent temperature and SLP biases over land, we first examine the simulated surface downward shortwave radiation and albedo, which control the energy budget of the land surface. CMIP5 and CFS models simulate excessive surface downward shortwave radiation over most of the NH continents during boreal summer in agreement with previous studies (Wild et al. 2015), while SINTEX exhibits reduced surface shortwave radiation in the northern high latitudes, but again excessive surface shortwave radiation over land between the Equator and 50°N compared to satellite estimates (Fig. 3). Obviously, the excessive downward surface shortwave radiation biases over the NH continents cannot explain the cold bias found over the same regions in the CGCMs during boreal summer (Fig. 2).

Numerous studies have found serious discrepancies between albedo observed from satellite products and simulated by CGCMs, but the focus has been mainly on the snow albedo feedback or the Arctic sea-ice albedo and their large spreads in CGCMs (Karlsson and Svenson 2013; Thackeray et al. 2015). For boreal summer, the land albedo modeled by CMIP3 models is systematically overestimated by as much as 5% despite most of the NH continents are snow-free during this season (Wang et al. 2006). Errors in total surface albedo for CMIP5, SINTEX and CFS models during boreal summer are presented in Figure 4. Despite many CMIP5 models being full Earth-System Models (Taylor et al. 2012), current

CGCMs continue to exhibit systematic positive albedo biases over the NH continents (Fig. 4) leading to improperly simulated land-sea temperature contrasts during boreal summer (Fig. 2). The positive bias is particularly strong over the NH high latitudes, the Tibetan Plateau and the Middle-East. Additionally, SINTEX and CFS also show important positive albedo biases over the Sahara (Fig. 4). Models have also important difficulties in simulating the strong gradients of surface albedo, especially over Africa north of the Equator.

Snow-free albedo is determined by surface characteristics, such as vegetation and soil composition, but also depends on the angular and spectral distributions of the incident solar flux (Stephens et al. 2015). In CGCMs, it is either totally prescribed, as a parameter dependent on land cover types, or partially simulated as an internal variable based on simplified radiative transfer schemes for vegetation and bare soils (Dickinson 1983). The snow-free land albedo parameterizations in SINTEX and CFS use prescribed tabulated background diffuse albedo values (see section2) and Figure 5, which displays errors in snow-free land background diffuse albedo for SINTEX and CFS models compared to MCD43GF-v5 product from MODIS, demonstrates that these prescribed values exhibit the same important positive biases as the modeled albedo during boreal summer (Fig. 4). This suggests that the table giving the correspondence between albedo and vegetation types and/or the classification of vegetation used to derive the albedo datasets in these models, are severely biased.

Climate models are very sensitive to the specification of the surface albedo since it is strongly affecting the radiation budget of the earth (Stephens et al. 2015). However, the hemispheric biases in TOA net radiation budget during boreal summer are very different in CFS and SINTEX despite of the similarity of the boreal summer rainfall dry biases over land in these two models (see Table 3). Moreover, CFS does not follow the paradigm that tropical rainfall must shift toward the relatively warmer hemisphere (Schneider et al. 2014). This suggests that a TOA hemispheric energetic framework as advocated in some studies (Haywood et al. 2016) is not sufficient to explain the rainfall biases in these two models. Nonetheless, monsoon systems are also driven by regional moist static energy and temperature contrasts between the ocean and continent (Dai et al. 2013; Nie et al. 2010) and even small errors in simulated land surface albedo may contribute significantly to the dry monsoon rainfall and cold temperature biases (Figs. 1 and 2). This close relationship between land albedo and the intensity of the monsoon is already illustrated by several studies, which used the land surface albedo as a tuning parameter to control the strength of the African and Asian summer monsoons (Richter et al. 2012; Kelly and Mapes 2013). In the next sections, we show through a large set of coupled model sensitivity experiments and an analysis of CMIP5 models that the tropical monsoon related rainfall biases are partly related to the skin temperature biases over land, especially over the NH subtropical desert regions.

4. Numerical experiments with global coupled models

4.a Assessing the role of land albedo through idealized numerical experiments

In order to illustrate the potential role of land albedo on the monsoon dry bias in current CGCMs, we examine first the response of the monsoon systems to an idealized modification by setting to zero everywhere the prescribed snow-free land diffuse albedo used in CFS and SINTEX (see section 2 and Table 2 for details). Obviously, these experiments (ZERO_CFS and ZERO_SINTEX, respectively) are designed to increase the land thermal forcing during boreal summer, which is significantly deficient in the two models as in CMIP5 models (Fig. 2). These experiments never represent the reality, but are useful to assess whether and how changes in land albedo affect tropical precipitation in state-of-the-art CGCMs.

The precipitation, temperature and TOA net radiation changes in these ZERO simulations are entirely consistent despite of the very different physical packages included in the two models (Fig. 6). Overall, the impact of a dark continent is to increase boreal summer precipitation over South and East Asia, and West Africa (Figs. 6a and d). This is especially true in ZERO_CFS where the ITCZ has shifted by about of 4° and is located around 10°N over the South Asia and West Africa regions (Fig. 7). Precipitation also increases over the eastern tropical Indian Ocean, maritime continent and at the mean position of the ITCZ in the tropical Pacific, but reduces significantly over the equatorial and South Pacific in the ZERO runs. Consistently, surface temperature and TOA net radiation substantially increase over the NH continents, especially over the subtropical deserts and the mid-latitudes (Figs. 6b-c and e-f). Thus, the ITCZ shifts in the hemisphere with greater atmospheric energy input, even if the main source of atmospheric heating is outside of the tropics (Kang et al. 2008; Frierson et al. 2013; Schneider et al. 2014; Voigt et al. 2014). This northward shift of the rain band is enough to completely reverse the land precipitation biases over West Africa and also to almost remove the dry bias over South Asia found in the standard versions of the models (a small negative bias of less than 1 mm/day is still there for CFS; see Fig. 8). Concerning the North American monsoon system, a large rainfall increase is also seen, but it is shifted westward over the Pacific Ocean in the two models instead over the land. This suggests that the regional rainfall anomalies over there are not controlled by the changes of the local albedo, but are a remote response to the enhanced African monsoon system to its east as manifested by the strong anticyclonic circulation over the western subtropical Atlantic (see Fig. 9 for details). This NH monsoon rainfall response is similar, but stronger, than in the idealized experiments performed by Haywood et al. (2016) for assessing the role of excessive SH energy (i.e. strong positive absorbed shortwave radiation bias) on the tropical rainfall biases in current CGCMs by equilibrating the hemispheric albedos. Intriguingly, the double ITCZ structure over the tropical Pacific is also significantly modified in the ZERO simulations, which experience a northward shift of tropical rainfall (Figs. 6a, d and 8).

The ZERO simulations, where the land albedo is constant, also illustrate the important role of the geometry of the continents and the orography in shaping the position of the core monsoon rainfall zones (Figs. 6a and d). The surface temperature response is generally consistent with the increase of absorbed solar energy by the surface, but with some important exceptions. Especially, a cooling is observed over the Sahel and Indo-Gangetic areas (Figs. 6b and e), which we attribute to the shift and strengthening of the monsoon and the resulting increase in cloud cover over these two areas (not shown).

The strong warming of the subtropics over land in the ZERO simulations (Figs. 6b-c and e-f) affects the large-scale monsoon circulation by enhancing the tropospheric temperature contrast between the continent and the adjacent oceans and also the associated vertical easterly shear (Dai et al. 2013). The low-level (850-hPa) circulation response in the ZERO experiments is dominated by enhanced cyclonic circulation over Africa, South and East Asia (more precisely over the arid regions adjacent to the core monsoon regions during boreal summer) and a related strengthening of the subtropical anticyclones to the East over the Pacific Ocean and to the West over the Atlantic Ocean (Figs. 9a and c). The close connection between the monsoons and the subtropical anticyclones (Rodwell and Hoskins 2001) is particularly exemplified on the western flank of the North Pacific anticyclone, where the moist tropical air moves poleward and feeds the East Asian monsoon. Consistent with a Kelvin-wave response, the equatorial easterlies are also greatly enhanced over the western and central equatorial Pacific (Gill 1980). Also, on the western flank of the monsoon cyclonic center over Africa, an enhanced equatorward flow and positive SLP anomalies are found over the North subtropical Atlantic. At the surface, the enhanced inter-hemispheric atmospheric transport in the ZERO simulations is dominated by the northward shift of the trade winds over the South Pacific, consistent with the strengthening of both the NH ITCZ and the South Pacific anticyclone, and, secondary only, by a slight increase of the inter-hemispheric atmospheric flux over the Atlantic Ocean (Figs. 9a and c). By contrast, a weakening of the Mascarene High and inter-hemispheric flux is found in the Indian sector despite of the large increase of rainfall over South Asia in the ZERO simulations.

The zonal asymmetry of the atmospheric response in the ZERO runs is even more evident in the velocity potential fields at 200-hPa (Figs. 9b and d). The monsoon rainfall improvements in the ZERO runs are actually driven by the east–west planetary differential heating since at 200-hPa the divergent centers over the subtropical continents match well the diabatic and sensible heating sources and are flanked by upper-level convergence centers over the tropical South Pacific on one side and the western Atlantic and South America on the other side. The robustness of this upper-level divergent circulation pattern is further attested by the similarity of the response in the two CGCMs. These upper-level centers are well coupled with the corresponding SLP centers of the same polarity in the low-level circulation (Figs. 9a and c), suggesting an important role of the interactions between the South Pacific subtropical anticyclone and the monsoonal heating for resolving the tropical rainfall biases during boreal summer in current CGCMs.

Hence, the atmospheric response to the change of the surface albedo in global CGCMs is very different from an uniform shift and strengthening of the Hadley circulation as found in aqua-planet or simple conceptual model simulations, which focus mostly on the annual mean circulation (Kang et al. 2008; Schneider et al. 2014; Voigt et al. 2014). The monsoon circulation changes in the ZERO runs are dominated by an enhancement of the zonal monsoon cyclone-subtropical anticyclone circulation driven by the east-west differential heating, as expected from the revised planetary scale perspective on summer monsoon circulation (Rodwell and Hoskins 2001; Chen 2003). Obviously, the complex land-sea geography of the NH induces important zonally asymmetric surface forcings (via surface heat fluxes and diabatic heating), which rectify drastically the atmospheric response in the ZERO runs through stationary Rossby-wave transport and Kelvin-wave response (Shaw et al. 2015). A simple regional Hadley cell argument cannot explain the strengthening of the subtropical anticyclones over the tropical Pacific in the boreal summer circulation as simulated in the ZERO runs (Rodwell and Hoskins 2001).

A caveat in these ZERO experiments is that we only replace a systematic dry bias in land precipitation with a systematic bias in other variables such as TOA net radiation and surface temperature (Figs. 6b-c and e-f; Tables 4 and 5) and also oceanic precipitation (Fig. 8). This type of compensating errors is very common in such idealized coupled experiments (Haywood et al. 2016). There is a deterioration of simulated boreal summer rainfall for many tropical regions in the ZERO runs compared to the control runs (Figs. 10a and d). The Root-Mean-Square Error (RMSE) and spatial pattern correlation with observed tropical rainfall during boreal summer deteriorate substantially from control to ZERO experiments in the two CGCMs, demonstrating that the ZERO simulations are less realistic than the control runs for the whole tropics (Table 4). However, the results bring forward the unexplored hypothesis that land albedo biases in the NH can be also potentially important to explain the dry monsoon biases in CGCMs.

4.b Using satellite land albedo improves the simulated tropical rainfall and atmospheric circulation

To demonstrate the realistic impact of revising the parameterization of snow-free albedo in SINTEX and CFS coupled models, we now compare the control simulations with simulations in which the prescribed snow-free land surface diffuse albedo in the two models has been replaced with corresponding satellite snow-free albedo estimates (MODIS_SINTEX and MODIS_CFS, respectively; see section 2 and Table 2). These changes really represent an update of the models in contrast to the idealized ZERO experiments described in the previous section.

First, using satellite snow-free diffuse albedo estimates instead of the prescribed and outdated diffuse albedo in the two CGCMs darkens the NH continents, enhances TOA net radiation at NH high- and subtropical-latitudes (Figs. 11a-b and e-f) and corrects parts of the surface cold temperature bias found in the control runs (e.g. compare Figs. 2b-c and Fig. 12).

Surface temperature improvements are significant over Asia and Africa, but less over North America suggesting that other important factors like the snow parameterization, the treatment of the orography and the roughness length parameterization may be dominant in this region (Fig. 12). Also the improvements in CFS are larger than in SINTEX, especially over the Sahara and Arabian regions, probably because the corrected biases in the background snow-free land albedo climatology used in CFS are much larger (see Fig. 5). Another possible reason is that the CFS albedo parameterization is more complex, with much more nonlinearities, since this model uses two different spectral bands and takes into account that the albedos for direct-beam and diffuse fluxes have different characteristics (see Section 2 for details). The darkening of the continents in the MODIS runs induces more rainfall over South and East Asia and West Africa as in the ZERO runs (Figs. 13a and e), but leads also to large-scale rainfall improvements for most tropical regions and in the SH (Figs. 10b and e). Furthermore, MODIS_CFS better represents both the magnitude and spatial patterns of summer monsoon precipitation over Africa and South Asia where major dry biases are seen in CFS (Fig. 10b and Table 4). The rectification of the mean-state is particularly significant over the Atlantic region where precipitation shift from the Gulf of Guinea to the continent (Fig. 13a) and for the zonal mean precipitation over the African-Asian domain (Fig. 7a). MODIS_SINTEX also shows improvements over South Asia, and in the tropical Atlantic, but the amplitude of the corrections is more modest (Fig. 10e and Table 4) consistent with the reduced albedo and temperature errors in SINTEX compared to CFS (Figs. 2b-c, 4b-c).

Consistent with these rainfall improvements, the monsoon low-level jet over the Arabian Sea and East Asia is strengthened (Figs. 13b and f). These changes are associated with a SLP decrease over Arabia, Middle-East and the Tibetan plateau, consistent with a stronger “heat” low over these regions. Over West Africa, the low-level equatorial easterlies and inland westerlies are significantly enhanced in MODIS_CFS compared to CFS, again in association with a stronger Sahara heat low during boreal summer (Fig. 13b). Similar, but more modest, changes in low-level winds are found in MODIS_SINTEX compared to SINTEX (Fig. 13f).

To further investigate the mechanism of the monsoon rainfall improvements, we now focus on the upper troposphere and its dominant dynamical feature during boreal summer, the Tropical Easterly Jet (TEJ; Wang 2006). The TEJ, located at about 200-hPa, 5°-25°N with core speeds in excess of 25 $m.s^{-1}$, stretches from Indochina to the tropical Atlantic. It develops because of the strong temperature gradient that exists between the (cold) equator and the (warm) subtropics in the upper troposphere during boreal summer associated with deep moist convection over Asia and Northwest Pacific (Chen 2003). The TEJ plays a paramount role in controlling the easterly vertical shear over developing weather disturbances off the Atlantic coast of Africa and in South Asia (Mishra and Salvekar 1980; Nicholson et al. 2007) and in driving the Asian monsoon (Jiang et al. 2004). The MODIS simulations show an increase in the extension and strength of the TEJ from the subtropical Pacific to the African continent compared to the control simulations (Figs. 13c and g) and better capture its observed extension (not shown). Overall, the mean easterly vertical wind shear between the lower and upper troposphere (e.g. the difference between zonal winds at 200- and 850-hPa) is greatly amplified over all monsoon regions in the MODIS runs compared to the control runs (Figs. 13b-c and f-g). All these features are consistent with the improved patterns of monsoon precipitation, which exhibit a greater northward extension during boreal summer in MODIS simulations. In turn, the enhanced diabatic heating associated with the Asian and African monsoons induces also stronger upper-level convergence to the East over the South Pacific and to its West over the Atlantic through the planetary-scale divergent circulation (Figs. 13d and h; Voigt et al. 2014; Hawcroft et al. 2017). As in the ZERO simulations, this contributes to strengthen the South Pacific anticyclone and reduce the eastward extension of the SPCZ (Figs. 13a-b and e-f). Moreover, all these changes are ultimately related to the differential surface thermal forcing (Figs. 11c and g) associated with the improvements of the surface albedo in the MODIS experiments (Figs. 11a and e).

The changes of the NH monsoons in the MODIS runs also induce a systematic strengthening of the SH subtropical anticyclones, which promotes blocking and stationary patterns at SH mid- and high-latitudes (Figs. 13b-c and f-g). This has robust implications for the SH, especially in the southern Pacific, where the surface temperature off the Antarctic coast (e.g. between 140°-60°W) warms significantly in the two models (Figs. 11c and g) due to latitudinal changes in ice limit (Figs. 11a and e). These SH changes are very beneficial for reducing rainfall biases in the SH subtropics and mid-latitudes (Figs. 10b and e). Surprisingly, these remote teleconnections also reduce the huge negative SLP biases found over the subtropics and mid-latitudes of the SH (in the form of an expanded trough; see Figs. 2b and c) in the control experiments. We will again visit this surprising result in the next section using CMIP5 models.

Interestingly, all these rainfall and atmospheric circulation improvements are not associated with significant changes of the RMSE and spatial correlation statistics for TOA net radiation at the global scale in the MODIS runs (Table 5). In line with recent studies

(Hawcroft et al. 2017; Kay et al. 2016), this suggests that a global or hemispheric energetic framework is not necessarily the best method to reduce the tropical rainfall biases in CGCMs.

4.c Seminal role of the heat lows over the subtropical deserts

Finally, the higher surface temperature, lower SLPs and stronger cyclonic circulation over the Sahara, Arabia and Middle-East arid regions in both the ZERO and MODIS simulations suggest additionally a more regional perspective related to a "heat low" mechanism to explain the improvements of the monsoons in these experiments (Cook and Vizy 2016; Lavaysse 2015; Lavaysse et al. 2016; Samson et al. 2016; Ashfaq et al. 2016). Due to the strong radiative cooling over arid regions, the role of these deserts is to decrease NH energy content and shift the ITCZ and the monsoon southward (Frierson et al. 2013). However, in the same energetic framework, the significant decrease of the surface albedo and associated increase of the TOA net radiation over these arid regions in our dedicated experiments (Figs. 11a-b and e-f) imply a northward shift of the mean precipitation (Figs. 13a and e). This shift is especially evident over the core monsoon zones in the ZERO and MODIS runs (Fig. 7). This seems ultimately related to improvements in the simulated surface temperature gradients between the monsoon zones over land, the neighboring arid regions (such as the Sahara and Middle-East deserts) and the ocean to the South (Fig. 12) and to a stronger sensible heat flux (Figs. 11d and h). Errors in prescribed snow-free diffuse albedo over the deserts (Fig. 5) may cause important biases in the computation of ground temperature (Fig. 12) and surface fluxes (Figs. 11d and h) because surface albedo regulates the shortwave radiation absorbed by the surface. These temperature and surface fluxes errors may in turn lead to erroneous SLP and circulation patterns (Figs. 13b-d and f-h), responsible for the dry biases in monsoon regions (Samson et al. 2016), apart from SST errors and incorrect global TOA net radiation imbalance in current CGCMs (Roehrig et al. 2013; Sandeep and Ajayamohan 2014; Haywood et al. 2016). This is in full agreement with the key-role attributed to the Sahara heat low for explaining the interannual and decadal variability of rainfall over West Africa, including the severe long-term Sahel drought during the 1970s and 1980s and its partial recovery during the recent decades (Cook and Vizy 2015; Lavaysse 2015; Lavaysse et al. 2016).

To further support the hypothesis that the NH subtropical deserts are an important factor in the rectification of the dry monsoon bias in CGCMs, we run two simulations similar to the MODIS runs, but with an additional artificial decrease of 0.2 of the surface diffuse albedo over the Sahara, Arabia and Middle-East deserts (referred as DESERT_CFS and DESERT_SINTEX; see Table 2). In both ZERO and MODIS experiments, the background snow-free surface albedo is changed everywhere, in an idealized way in the ZERO experiments and realistically in MODIS experiments. In both of them, the observed monsoon changes seem to be linked to skin temperature and SLP changes over the hot subtropical desert extending from West Africa to Pakistan and northwest India. However, an exact quantification is difficult since the background snow-free albedo has been changed elsewhere compared to the control runs. On the other hand, in the DESERT experiments, the only modification compared to the MODIS runs is a change in the background snow-free surface albedo over the NH subtropical desert. So accordingly, the DESERT experiments by construction are designed to provide a more precise quantification of the relationship between the strength of the monsoon systems, essentially the African and South Asian monsoon systems, and climate conditions over the neighboring subtropical deserts.

Due to this artificial albedo decrease, these arid regions absorb more shortwave radiation and, as expected, the skin temperature, upward long-wave and sensible heat fluxes are substantially enhanced compared to the MODIS simulations (Figs. 14a-b and e-f). The increased sensible heat flux and associated heating of the lower atmosphere are sufficient to decrease furthermore the surface pressure and enhance the cyclonic vorticity over these regions compared to the MODIS simulations (Figs. 14d and h). In both models, the region of warm temperatures is more zonally coherent and manifests itself as a zonally elongated heat trough extending from the Sahara to the Middle-East in the simulated SLP fields (Figs. 14d and h). The response of the NH monsoons to the enhanced large-scale north-south SLP gradient that occurs across Africa and Asia, associated with this planetary-scale heat low, is illustrated in the large-scale circulation and precipitation fields simulated in the DESERT runs (Figs. 14c-d and g-h). In DESERT runs, the ITCZ shifts northward compared to MODIS experiments (Fig. 7), the dry bias over West Africa is again reversed into a wet bias, as in the ZERO simulations, and the rainfall over South Asia is only slightly underestimated (Fig. 15). Furthermore, a significant duality between the diabatic heating associated with the African-Asian monsoon and the strength of the subtropical anticyclones over the Pacific and Atlantic oceans is also found, as in the ZERO experiments (Figs. 14d and h). As a direct consequence, the North American monsoon is, however, decreased. In these areas, a large increase of rainfall is seen, but it is shifted westward over the Pacific Ocean in the two models (Figs. 14c and g). The SLP and 850 hPa wind responses in the DESERT experiments confirm that the drying of the North American monsoon and this westward shift of the rain band are both associated with the strengthening of the North Atlantic subtropical anticyclone, which is remotely forced by diabatic heating associated with the African-Asian monsoon (Figs. 14d and h; Rodwell and Hoskins 2001; Rodwell and Hoskins 1996). Finally, the similarity in large-scale circulation and rainfall responses in the two models (Figs. 14c-d and g-h) and the large-scale rainfall improvements in the DESERT runs (Figs. 10c and f) demonstrate the robustness of the role of the NH deserts on the boreal summer climate.

A large majority of CMIP5 models also exhibit a severe cold bias over the NH subtropical deserts, as CFS and SINTEX (Fig. 16a). A substantial co-variability also exists between this NH subtropical desert temperature and atmospheric variability in CMIP5 models as revealed by composite differences for precipitation, SLP and 850-hPa wind between the six warmest and six coldest CMIP5 models (Figs. 16b and c) and regression between tropical rainfall and NH deserts surface temperature across 36 CMIP5 models (Fig. 17). The selected six coldest and warmest CMIP5 models used in this composite analysis are, respectively, the six CMIP5 models with the highest (lowest) boreal summer land surface temperature in the domain 15°-40°N and 20°W-75°E, which was used in our DESERT numerical experiments. They correspond to the CMIP5 models, respectively, on the extreme left and right of the plot displayed in Fig. 16a. The composite and regression results show similar rainfall and atmospheric circulation responses over the West African and South Asian monsoon regions as observed improvements in DESERT, ZERO and MODIS experiments with respect to their control experiments (see Figs. 9, 13 and 14). They also show a consistent relationship between the surface temperature over the NH subtropical deserts and the SLP variability over the subtropics and mid-latitudes of the SH during boreal summer (Fig. 16c), as our numerical experiments, suggesting again that the large negative SLP biases found over the SH subtropics and mid-latitudes in CMIP5 models (Fig. 2a) may have remote origins in the NH.

However, the CMIP5 results do not show a westward shift of the North American monsoon as in the ZERO and DESERT experiments (Figs. 14c and d). Over this region, the CMIP5 rainfall pattern is more similar to the North American monsoon rainfall response in the MODIS experiments, which seems to be more realistic (Figs. 13a and e). Furthermore, the rainfall regression pattern from CMIP5 models shows also a reduction of the double ITCZ over the tropical Pacific compared to our ZERO and DESERT experiments, with a decrease of the rainfall biases north of the equator (Fig. 17), while our experiments show in most cases a more intense ITCZ and a stronger wet bias in the North tropical Pacific (Figs. 6a and d, 14c and g).

Despite of these differences, these results demonstrate that a change of surface albedo and skin temperature over the NH subtropical deserts may lead on its own to an important rectification of the ITCZ position in monsoon regions, significant atmospheric improvements over the SH (in subtropics and mid-latitudes of the SH) and a modest reduction of the Pacific double ITCZ during boreal summer in current CGCMs. Finally, the similarity in large-scale circulation and rainfall response in our two models demonstrates the robustness of the role of the NH deserts on the boreal summer climate.

5. Conclusion and discussion

In a very broad sense, our modeling efforts demonstrate that the monsoon dry biases over the Afro-Asian region in current CGCMs are, partly, related to improper simulation of the large-scale pressure gradient between the hot NH subtropical deserts and the relatively cooler oceans to the South. Our results further highlight that erroneous meridional and zonal surface temperature gradients over the monsoon regions in current CGCMs, while partly forced by atmospheric and convection errors, are also able to drive atmospheric and rainfall biases, especially away from the Equator, by geostrophic adjustments. While previous studies have mostly focused on the role of SST biases (Roehrig et al. 2013; Prodhomme et al. 2014; Reichler and Kim 2008; Bollasina et Ming 2013; Levine et al. 2013), here we have tested the land albedo contribution to these erroneous temperature gradients and showed the associated impact on the monsoon rainfall and circulation biases, a topic rarely discussed thoroughly in the literature. This extends and is consistent with recent studies focusing more specifically on the Indian monsoon using a tropical channel coupled model (Samson et al. 2016) or an atmospheric model (Ashfaq et al. 2016). The variability of the heat lows over the NH subtropical arid regions is demonstrated to modulate significantly the thermal and SLP contrasts between ocean and land in our two coupled models. In most CMIP5 models, this thermal contrast between the NH deserts and the oceans is considerably reduced due to weak surface thermal forcing over land (Figs. 2a and 16a), which results in higher-than observed surface pressures (i.e., the lows are not as deep as observed; Fig. 16c). CMIP5 models also assert that the stronger the surface thermal forcing over the deserts is, the weaker are the dry bias over the NH monsoon regions and the Pacific double ITCZ problem during boreal summer (Figs. 16b and 17). Furthermore, the darkening of the NH arid regions in our experiments highlights the significant duality between the NH monsoons and the subtropical anticyclones over the Pacific and Atlantic oceans and is demonstrated to play a significant role in correcting SH rainfall and SLP biases in current coupled models. Indeed, in all our experiments, the Sahara, Arabia and Middle-East regions form a planetary-scale thermal low, which exhibits a clear connection to the summertime Asian and African monsoon circulations and the strength of the South Pacific anticyclone. Preliminary analysis shows that similar large-scale improvements can be expected for the SH monsoon systems and the double ITCZ problem during boreal winter (not shown).

This suggests that the contribution of the land and subtropical deserts to the thermal forcing of the tropical climate is significantly underestimated in current CGCMs. Part of this bias results from incorrect albedo parameterization, but this by no means precludes the importance of other sources of errors concerning the land emissivity or roughness length, which regulate the skin temperature over the deserts through the balance between the upward long-wave and sensible heat fluxes (Deardorff 1978) or the soil characteristics and humidity, which modulate the temperature gradient between the monsoon zones and the adjacent deserts (Kumar et al. 2014).

Unfortunately, the energy budget over these arid regions is still afflicted with considerable uncertainties, especially the poorly known sensible heat fluxes, which are often obtained as residual terms from the best estimates for downward solar and thermal radiation (Wild et al. 2015). Due to their key importance for monsoon climates and tropical rainfall biases in CGCMs, the energy budget and sensible heat flux over land must deserve more attention. Understanding land processes, as well as their coupling to the large-scale circulation, and improving their parameterization in current CGCMs must be considered as one of the current grand challenges in climate science at the same level than the cloud-radiative feedbacks and the convection (Bony et al. 2015).

Acknowledgments

The authors gratefully acknowledge the financial support given by the Earth System Science Organization, Ministry of Earth Sciences, Government of India, to conduct this research under the National Monsoon Mission (Grant #MM/SERP/CNRS/2013/INT-10/002, Contribution #MM/PASCAL/RP/08). We sincerely thank Prof. Ravi Nanjundiah, Director, Indian Institute of Tropical Meteorology (IITM, India) and Dr. R Krishnan, executive Director, Centre for Climate Change Research (at IITM, India) for all the support during this research study. We acknowledge the World Climate Research Programme's Working Group on Coupled Modeling, which is responsible for CMIP, and we thank the climate modeling groups (listed in the Supplementary Materials) for producing and making available their model output. For CMIP, the US Department of Energy's Program for Climate Model Diagnosis and Inter-comparison provides coordinating support and led development of software infrastructure in partnership with the Global Organization for Earth System Science Portals. Computer resources from Indian Institute of Tropical Meteorology (India) and GENCI-IDRIS (France, Grants 2015, 2016, 2017 – 016895) are also acknowledged.

References

Alessandri A, Gualdi S, Polcher J, Navarra A (2007) Effects of land surface-vegetation on the boreal summer surface climate of a GCM. *J. Clim.* **20**:255-278.

Annamalai H *et al.* (2015) Persistence of Systematic errors in the Asian-Australian monsoon Precipitation in climate models: a way forward. *Clivar Exchanges* **66**:19-22.

Ashfaq M, Rastogi D, Mei R, Touma D, Leung RL (2016) Sources of errors in the simulation of south Asian summer monsoon in CMIP5 GCMs. *Clim. Dyn.* online, doi 10.1007/s00382-016-3337-7

Biasutti M (2013) Forced Sahel rainfall trends in the CMIP5 archive. *J. Geophys. Res.* **118**:1613–1623.

Bollasina MA, Ming Y (2013) The general circulation model precipitation bias over the southwestern equatorial Indian Ocean and its implications for simulating the South Asian monsoon. *Clim. Dyn.* **40**:823–838.

Bony S *et al.* (2015) Clouds, circulation and climate sensitivity. *Nat. Geosci.* **8**:261–268.

Boos WR and Kuang Z (2010) Dominant control of the South Asian monsoon by orographic insulation versus plateau heating. *Nature* **463**:218–222.

Boos WR and Hurley JV (2013) Thermodynamic Bias in the Multimodel Mean Boreal Summer Monsoon. *J. Climate* **26**:2279–2287.

Chakraborty A (2002) Role of Asian and African orography in Indian summer monsoon. *Geophys. Res. Lett.* **29**:1989.

Charney J, Quirk WJ, Chow S, Kornfield J (1977) A Comparative Study of the Effects of Albedo Change on Drought in Semi–Arid Regions. *J. Atmos. Sci.* **34**:1366–1385.

Chen T-C (2003) Maintenance of Summer Monsoon Circulations: A Planetary-Scale Perspective. *J. Climate* **16**:2022-2037.

Cook KH, Vizy EK (2015) Detection and analysis of an amplified warming of the Sahara desert. *J. Climate* **28**:6560–6580.

Dai A (2006) Precipitation characteristics in eighteen coupled climate models. *J. Climate* **19**:4605–4630.

Dai A *et al.* (2013) The relative roles of upper and lower tropospheric thermal contrasts and tropical influences in driving Asian summer monsoons. *J. Geophys. Res.* **118**:7024–7045.

Deardorff JW (1978) Efficient prediction of ground surface temperature and moisture with inclusion of a layer of vegetation. *J. Geophys. Res.* **83**:1889–1903.Dickinson RE (1983)

Land Surface Processes and Climate Surface Albedos and Energy-Balance. Adv. Geophys. **25**:305-353.

Dee DP *et al.* (2011) The ERA-Interim reanalysis: Configuration and performance of the data assimilation system. *Q. J. Roy. Meteorol. Soc.* **137**:553–597.

Dirmeyer PA (1998) Land-sea geometry and its effect on monsoon circulations. *J. Geophys. Res.* **103**(D10):11,555-11,572.

Doi T, Behera SK, Yamagata T (2016) Improved seasonal prediction using the SINTEX-F2 coupled model. Extended ENSO predictions using a fully coupled ocean–atmosphere model. *JAMES, online*.

Frierson DM *et al.* (2013) Contribution of ocean overturning circulation to tropical rainfall peak in the Northern Hemisphere. *Nat. Geosci.* **6**:940–944.

Gill AE (1980) Some simple solutions for heat-induced tropical circulation. *Q. J. Roy. Meteorol. Soc.* **106**:447–462.

Goswami BB, M Deshpande, P Mukhopadhyay, SK Saha, SA Rao, R Murthugudde, BN Goswami (2014) Simulation of monsoon intraseasonal variability in NCEP CFSv2 and its role on systematic bias. *Clim. Dyn.* 43:2725–2745

Hawcroft M, Haywood J, Collins M, Jones A, Jones AC, Stephens G. (2017) Southern albedo, interhemispheric energy transports and the ITCZ: global impacts of biases in a coupled model. *Clim. Dyn.* 48:2279–2295.

Haywood JM *et al.* (2016) The impact of equilibrating hemispheric albedos on tropical performance in the HadGEM2-ES coupled climate model, *Geophys. Res. Lett.* **43**:395–403.

Hou Y-T, Moorthi S, Campana KA (2002) Parameterization of solar radiation transfer in the NCEP models. NCEP Office Note 441.Hourdin F, Gainusa-Bogdan A, Braconnot P, Dufresne J-L, Traore A-K, Rio C (2015) Air moisture control on ocean surface temperature, hidden key to the warm bias enigma. *Geophys. Res. Lett.* **42**:10,885–10,893.

Houldcroft CJ, Grey WMF, Barnsley M, Taylor CM, Los SO, North PRJ (2009) New vegetation albedo parameters and global fields of soil background albedo derived from MODIS for use in a climate model. *J. of Hydrometeorology*, **10**:183–198

Huffman GJ, Adler RF, Bolvin DT, Gu G (2009) Improving the global precipitation record: GPCP Version 2.1. *Geophys. Res. Lett.* **36**:L17808.

IPCC Fifth Assessment Report of the Intergovernmental Panel on Climate Change (2013) www.ipcc.ch/ipccreports/ar4-wg1.htm.

Jiang XN, Li T, Wang B (2004) Structures and mechanisms of the northward propagating boreal summer intraseasonal oscillation. *J. Climate* **17**:1022–1039.

Johnson SJ, Levine RC, Turner AG et al. (2016) The resolution sensitivity of the South Asian monsoon and Indo-Pacific in a global _0.35° AGCM. *Clim. Dyn.* **46**:807-831. doi:10.1007/s00382-015-2614-1

Kang SM, Held IM, Frierson DMW, Zhao M (2008) The response of the ITCZ to extratropical thermal forcing: Idealized slab-ocean experiments with a GCM. *J. Climate* **21**:3521–3532.

Karlsson J, Svenson G (2013) Consequences of poor representation of Arctic sea-ice albedo and cloud-radiation interactions in the CMIP5 model ensemble. *Geophys. Res. Lett.* **40**:4374–4379.

Kato S *et al.* (2013) Surface Irradiances Consistent with CERES-Derived Top-of-Atmosphere Shortwave and Longwave Irradiances. *J. Climate* **26**:2719–2740.

Kay JE, Wall C, Yettella V, Medeiros B, Hannay C, Caldwell P, Bitz C. (2016) Global climate impacts of fixing the Southern Ocean shortwave radiation bias in the Community Earth System Model. *J. Clim.* **29**:4617-4636, doi:10.1175/JCLI-D-15-0358.1

Kelly P, Mapes B (2010) Land Surface Heating and the North American Monsoon Anticyclone: Model Evaluation from Diurnal to Seasonal. *J. Climate* **23**:4096–4106.

Kelly P, Mapes B (2013) Asian monsoon forcing of subtropical easterlies in the Community Atmosphere Model: Summer climate implications for the western Atlantic. *J. Climate* **26**:2741–2755.

Kim HM, Webster PJ, Curry JA, Toma VE (2013) Asian summer monsoon prediction in ECMWF system 4 and NCEP CFSv2 retrospective seasonal forecasts. *Clim. Dyn.* **39**:2975–2991.

Kumar P, Podzun R, Hagemann S, Jacob D (2014) Impact of modified soil thermal characteristic on the simulated monsoon climate over south Asia. *J. Earth Syst. Sci.* **123**:151–160.

Lavaysse C (2015) Warming trends: Saharan desert warming. *Nat. Clim. Change* **5**:807–808.

Lavaysse C, Flamant C, Evan A, Janicot S, Gaetani, M (2016) Recent climatological trend of the Saharan heat low and its impact on the West African climate. *Clim. Dyn.* 47: 3479–3498.

Levine RC, Turner AG, Marathayil D, Martin GM (2013) The role of northern Arabian Sea surface temperature biases in CMIP5 model simulations and future predictions of Indian summer monsoon rainfall. *Clim. Dyn.* **41**:155-172.

Liang X, Liu Y, Wu G (2005a) The role of land-sea distribution in the formation of the Asian summer monsoon. *Geophys. Res. Lett.* **32**:L03708.

Liang X-Z et al. (2005b), Development of land surface albedo parameterization based on Moderate Resolution Imaging Spectroradiometer (MODIS) data. *J. Geophys. Res.* 110:D11107, doi:10.1029/2004JD005579

Lin JL (2007) The double-ITCZ problem in IPCC AR4 coupled GCMs: Ocean-atmosphere feedback analysis. *J. Climate* **20**:4497–4525.

Loeb NG *et al.* (2012) Advances in understanding top-of-atmosphere radiation variability from satellite observations. *Surv. Geophys.* **33**, 359–385.

Masson S, Terray P, Madec G, Luo J–J, Yamagata T, Takahashi K (2012) Impact of intra-daily SST variability on ENSO characteristics in a coupled model. *Clim. Dyn.* **39**:681-707.

Mishra SK, Salvekar PS (1980) Role of barotropic instability in the development of monsoon disturbances. *J. Atmos. Sci.* **37**:383–394.

Nicholson SE, Barcilon AI, Challa M, Baum M (2007) Wave Activity on the Tropical Easterly Jet. *J. Atmos. Sci.* **64**:2756-2763.

Nie J, Boos WR, Kuang Z (2010) Observational evaluation of a convective quasi-equilibrium view of monsoons. *J. Climate* **23**:4416–4428.

Noreen EW (1989) Computer-intensive methods for testing hypotheses: an introduction. Wiley, New York

Prodhomme C *et al.* (2014) Impacts of Indian Ocean SST biases on the Indian Monsoon: as simulated in a global coupled model. *Clim. Dyn.* **42**:271–290.

Prodhomme C *et al.* (2016) Benefits of increasing the model resolution for the seasonal forecast quality in EC-Earth. *J. Climate* online.

Rai A, Saha SK (2017) Evaluation of energy fluxes in the NCEP climate forecast system version 2.0 (CFSv2). *Clim. Dyn.* online, doi:10.1007/s00382-017-3587-z

Reichler T, Kim J (2008) How well do coupled models simulate today's climate? *Bull. Amer. Meteorol. Soc.* **89**:303–311.

Richter I, Xie S-P, Wittenberg AT, Masumoto Y (2012) Tropical Atlantic biases and their relation to surface wind stress and terrestrial precipitation. *Clim. Dyn.* **38**:985–1001.

Richter I (2015) Climate model biases in the eastern tropical oceans: Causes, impacts and ways forward. Clim. Change **6**:345–358.

Rodwell MJ, Hoskins BJ (1996) Monsoons and the dynamics of deserts. *Q. J. Roy. Meteorol. Soc.* **122**:1385–1404.

Rodwell MJ, Hoskins BJ (2001) Subtropical Anticyclones and Summer Monsoons. *J. Climate* **14**:3192-3211.

Roeckner E *et al.* (2003) The atmospheric general circulation model ECHAM5: Part 1: model description. Max-Planck-Institut fur Meteorologie, Hamburg, MPI-Report 349.

Roehrig R, Bouniol D, Guichard F, Hourdin F, Redelsperger JL (2013) The Present and Future of the West African Monsoon: A Process-Oriented Assessment of CMIP5 simulations along the AMMA Transect. *J. Climate* **26**:6471- 6505.

Sabeerali CT, Rao SA, Dhakate AR, Salunke K, Goswami BN (2015) Why ensemble mean projection of south Asian monsoon rainfall by CMIP5 models is not reliable? *Clim. Dyn.* **45**:161–174.

Saha S *et al.* (2014) The NCEP climate forecast system version 2. *J. Climate* **27**:2185–2208.

Samson G, Masson S, Durand F, Terray P, Berthet S, Jullien S (2016) Role of land surface albedo and horizontal resolution on the Indian Summer Monsoon biases in a coupled ocean-atmosphere tropical-channel model. *Clim. Dyn.* online.

Sandeep S, Ajayamohan RS (2014) Origin of the cold bias over the Arabian Sea in climate models. *Scientific Reports*, **4**:6043.

Schaaf CB, Liu J, Gao F, Strahler AH (2011) Land Remote Sensing and Global Environmental Change. *L. Remote Sens. Glob. Environ. Chang.* **11**:549–561.

Schneider T, Bischoff T, Haug GH (2014) Migration and dynamics of the inter-tropical convergence zone. *Nature* **513**:45–53.

Shaw TA, Voigt A, Kang SM, Seo J (2015) Response of the intertropical convergence zone to zonally asymmetric subtropical surface forcings. *Geophys. Res. Lett.* **42**:9961–9969.

Sooraj KP, Terray P, Mujumdar M (2015) Global warming and the weakening of the Asian summer monsoon circulation: assessments from the CMIP5 models. *Clim. Dyn.* **45**:233–252.

Sperber KR *et al.* (2013) The Asian summer monsoon: an inter-comparison of CMIP5 vs. CMIP3 simulations of the late 20th century. *Clim. Dyn.* **41**:2711–2744.

Stephens GL *et al.* (2010) Dreary state of precipitation in global models. *J. Geophys. Res.* **115**:D24211.

Stephens GL, O'Brien D, Webster PJ, Pilewski P, Kato S, Li J-I (2015) The Albedo of Earth. *Rev. Geophys.* **53**:141–163.

Sud YC, Smith WE (1985) Influence of local land surface processes on the Indian Monsoon: A numerical study. *J. Climate and Appl. Meteor.* **24**:1015-1036.

Swapna et al. (2015) The IITM earth system model. *Bull. Amer. Meteor. Soc.* **96**:1351-1367 doi:10.1175/BAMS-D-13-00276.1

Taylor KE, Stouffer RJ, Meehl GA (2012) An overview of CMIP5 and the experiment design. *Bull. Amer. Meteorol. Soc.* **93**:485–498.

Terray P, Delecluse P, Labattu S, Terray L (2003) Sea Surface Temperature Associations with the Late Indian Summer Monsoon. Clim. Dyn. **21**:593–618

Thackeray CW, Fletcher CG, Derksen C (2015) Quantifying the skill of CMIP5 models in simulating seasonal albedo and snow cover evolution, *J. Geophys. Res.* **120**:5831–5849.

Vamborg FSE, Brovkin V, Claussen M (2014) Background albedo dynamics improve simulated precipitation variability in the Sahel region. *Earth Syst. Dynam.* **5**:89-101

Voigt A, Stevens B, Bader J, Mauritsen, T (2014) Compensation of hemispheric albedo asymmetries by shifts of the ITCZ and tropical clouds, *J. Climate* **27**:1029–1045.

Wang B (2006) *The Asian monsoon*. Springer-Verlag 870 pp.

Wang C, Zhang L, Lee SK, Wu L, Mechoso CR (2014) A global perspective on CMIP5 climate model biases. *Nat. Clim. Change.* **4**:201–205.

Wang S, Trishchenko AP, Khlopenkov KV, Davidson A (2006) Comparison of International Panel on Climate Change Fourth Assessment Report climate model simulations of surface albedo with satellite products over northern latitudes, *J. Geophys. Res.* **111**:D21108.

Wild M *et al.* (2015) The energy balance over land and oceans: an assessment based on direct observations and CMIP5 climate models. *Clim. Dyn.* **44**:3393–3429.

Wu G *et al.* (2012) Thermal Controls on the Asian Summer Monsoon. *Scientific Rep.* **2**:1–7.

Xie, P, Arkin,PA (1997) Global precipitation: A 17-year monthly analysis based on gauge observations, satellite estimates, and numerical model outputs. *Bull. Amer. Meteor. Soc.* **78**:2539–2558

Yang F, Mitchell K, Hou Y-T, Dai Y, Zeng X, Wang Z, Liang X-Z (2008) Dependence of Land Surface Albedo on Solar Zenith Angle: Observations and Model Parameterization. *J. Appl. Meteo. Clim.* **47**:2963-2982.

Yin et al. (2004) Comparison of the GPCP and CMAP Merged Gauge–Satellite Monthly Precipitation Products for the Period 1979–2001. *J. of Hydrometeorology* **5**:1207-1222

Figure Captions

Figure 1: Rainfall biases (mm/day, shading) during boreal summer (e.g. from June to September) in **(a)** ensemble-mean from 36 CMIP5 CGCMs (see **Table 1**), **(b)** SINTEX-F2 coupled model (Masson et al. 2012) and **(c)** Climate Forecast System version2 (CFS) coupled model (Saha et al. 2014) against monthly-accumulated precipitation from the Global Precipitation Climatology Project (Huffman et al. 2009) over the 1979-2010 period. The boreal summer rainfall standard deviation in the 36 CMIP5 CGCMs is also shown as contours (interval every 0.5 mm/day) in panel **(a)**.

Figure 2: Skin temperature (°C, shading) and SLP (hPa, contours every 1-hPa) biases during boreal summer (e.g. from June to September) in **(a)** ensemble-mean from 36 CMIP5 CGCMs (see **Table 1**), **(b)** SINTEX coupled model and **(c)** CFS coupled model against ERA-Interim reanalysis estimates (Dee et al. 2011) over the 1979-2014 period.

Figure 3: Surface downward shortwave radiation biases (W/m^2) during boreal summer (e.g. from June to September) in **(a)** ensemble-mean from 36 CMIP5 CGCMs (see **Table 1**), **(b)** SINTEX and **(c)** CFS coupled models against estimates from the CERES-EBAF version 2.8 dataset (Kato et al. 2013). The CERES_EBAF boreal summer climatology is estimated from the period 2000-2014.

Figure 4: Surface albedo biases (%) during boreal summer (e.g. from June to September) in **(a)** ensemble-mean from 36 CMIP5 CGCMs (see **Table 1**), **(b)** SINTEX coupled model and **(c)** CFS coupled model against radiative fluxes estimates computed from the Clouds and Earth's Radiant Energy System (CERES) system (Kato et al. 2013) over the 2000-2014 period.

Figure 5: Background snow-free albedo biases (%) over land during boreal summer (e.g. from June to September) for **(a)** diffuse broadband Short-Wave (SW, 0.3–5.0 μm) albedo in SINTEX CGCM, **(b)** diffuse Near-Infra-Red (NIR, >0.7 μm) albedo in CFS CGCM and **(c)** diffuse Visible (VIS, <0.7 μm) albedo in CFS CGCM against corresponding estimates from the Moderate Resolution Imaging Spectro-radiometer (MODIS) snow-free gap-filled white-sky (diffuse) albedo product MCD43GF-v5 (Schaaf et al. 2011). The MODIS climatologies are estimated from the 2003-2013 period. See section 2 for further details.

Figure 6: Boreal summer (e.g. from June to September) differences between the ZERO and control experiments (see **Table 2**) for CFS (**a**,**b**,**c**) and SINTEX (**d**,**e**,**f**) models. For **(a,d)** precipitation (mm/day), **(b,e)** surface skin temperature (°C) and **(c,f)** Top Of Atmosphere (TOA) net shortwave radiation (W/m^2). In panels (**a**) and (**b**), differences that are above the 95% confidence level according to a permutation procedure with 9999 shuffles are encircled. In the other panels, the maps only show differences, which are above the 95% confidence level.

Figure 7: **(a)** Boreal summer (e.g. from June to September) zonal mean precipitation (mm/day) over an African-Asian domain (70°W-100°E) in the different CFS simulations (see **Table 2**) against monthly-accumulated precipitation from the Global Precipitation Climatology Project (Huffman et al. 2009) over the 1979-2010 period, **(b)** as in panel **(a)**, but for the SINTEX simulations (see **Table 2**).

Figure 8: Rainfall biases (mm/day) during boreal summer (e.g. from June to September) in **(a)** ZERO_SINTEX experiment (see **Table 2**) and **(b)** ZERO_CFS experiment (see **Table 2**) against monthly-accumulated precipitation from the Global Precipitation Climatology Project (Huffman et al. 2009) over the 1979-2010 period.

Figure 9: Boreal summer (e.g. from June to September) differences between the ZERO and control experiments (see **Table 2**) for CFS **(a,b)** and SINTEX **(c,d)** models. For **(a,c)** 850-hPa winds (m/s) and Sea Level Pressure (hPa) and **(b,d)** 200-hPa velocity potential (10^{-6} m^2/s). SLP and 200-hPa velocity potential differences, which are above the 95% confidence level according to a permutation procedure with 9999 shuffles, are encircled. In panels (**a**) and (**c**), the maps only show the 850-hPa wind differences, which are above the 95% confidence level.

Figure 10: Improvement or deterioration of simulated tropical rainfall during boreal summer in the different experiments (e.g. ZERO, MODIS, DESERT) compared to the biases in the control simulation for each model (e.g. CFS and SINTEX). Following Haywood et al. (2016), for each model, the improvement/deterioration for ZERO, MODIS and DESERT experiments with respect to the control simulation is computed as 1 – abs((EXP-GPCP)/(CTL-GPCP)), where EXP is either ZERO, MODIS or DESERT, GPCP is the boreal summer rainfall

climatology for the 1979-2010 period and CTL is the corresponding control simulation. In this way, positive values represent the percentage improvement in boreal summer rainfall (and are bounded by 1) and negative values represent the degradation in boreal summer rainfall compared to the control simulation. **(a)** Boreal summer rainfall improvement or degradation in ZERO_CFS with respect to CFS, **(b)** Boreal summer rainfall improvement or degradation in MODIS_CFS with respect to CFS and **(c)** Boreal summer rainfall improvement or degradation in DESERT_CFS with respect to CFS. **(d)**, **(e)** and **(f)** as **(a)**, **(b)** and **(c)**, respectively, but for SINTEX model.

Figure 11: Boreal summer (e.g. from June to September) differences between the MODIS and control experiments (see **Table 2**) for CFS **(a,b,c,d)** and SINTEX **(e,f,g,h)** models. For **(a,e)** albedo (%), **(b,f)** Top Of Atmosphere (TOA) net shortwave radiation (W/m^2), **(c,g)** skin temperature (°C) and **(d,h)** sensible heat flux (W/m^2). The maps only show differences, which are above the 95% confidence level according to a permutation procedure with 9999 shuffles.

Figure 12: Surface temperature biases (°C) during boreal summer (e.g. from June to September) in **(a)** MODIS_SINTEX experiment (see **Table 2**) and **(b)** MODIS_CFS experiment (see **Table 2**) against ERA-Interim reanalysis climatology (Dee et al. 2011) over the 1979-2014 period.

Figure 13: Boreal summer (e.g. from June to September) differences between the MODIS and control experiments (see **Table 2**) for CFS **(a,b,c,d)** and SINTEX **(e,f,g,h)** models. For **(a,e)** precipitation (mm/day), **(b,f)** 850-hPa winds (m/s) and SLP (hPa), **(c,g)** 200-hPa winds (m/s) and 200-hPa stream function (10^{-6} m^2/s) and **(d,h)** 200-hPa velocity potential (10^{-6} m^2/s). In panels **(c)** and **(g)**, positive (negative) values of the stream function denote clockwise (anticlockwise) motions. Precipitation, SLP, 200-hPa stream function and 200-hPa velocity potential differences, which are above the 95% confidence level according to a permutation procedure with 9999 shuffles are encircled. In panels (**b**), (**c**), (**e**) and (**f**), the maps only show the 850 and 200-hPa wind differences, which are above the 95% confidence level.

Figure 14: Boreal summer (e.g. from June to September) differences between the DESERT and MODIS experiments (see **Table 2**) for CFS **(a,b,c,d)** and SINTEX **(e,f,g,h)** models. For

(a,e) skin temperature (°C), **(b,f)** sensible heat flux (W/m^2), **(c,g)** precipitation (mm/day) and **(d,h)** 850-hPa winds (m/s) and Sea Level Pressure (hPa). In panels (**a**), (**b**), (**e**) and (**f**), the maps only show differences, which are above the 95% confidence level according to a permutation procedure with 9999 shuffles. In panels (**c**), (**d**), (**g**) and (**h**), precipitation and SLP differences, which are above the 95% confidence level are encircled and 850-hPa wind differences are shown only if they are above the 95% confidence level.

Figure 15: Rainfall biases (mm/day) during boreal summer (e.g. from June to September) in **(a)** DESERT_SINTEX experiment (see **Table 2**) and **(b)** DESERT_CFS experiment (see **Table 2**) against monthly-accumulated precipitation from the Global Precipitation Climatology Project (Huffman et al. 2009) over the 1979-2010 period.

Figure 16: (a) Surface temperature bias (°C) during boreal summer over the same domain (land only: latitude 15°-40°N, longitude 20°W-75°E) as used in the DESERT experiments for 36 CMIP5 models with respect to surface temperature climatology estimated from ERA-Interim reanalysis (Dee et al. 2011) over the 1979-2014 period, **(b)** Rainfall (mm/day) composite differences between the six warmest and six coldest CMIP5 models over the NH subtropical deserts, and **(c),** same as (**b**), but for SLP (hPa) and 850-hPa winds (m/s) composite differences. The six CMIP5 models with the highest (lowest) boreal summer land surface temperature over the NH subtropical deserts (15°-40°N, 20°W-75°E) correspond, respectively, to the CMIP5 models on the extreme right and left of the plot displayed in panel **(a)**.

Figure 17: linear regression between rainfall (mm/day) and the surface temperature (°C) over the NH subtropical desert (15°-40°N, 20°W-75°E) in 36 CMIP5 models**.** Regression coefficients significant at the 90% confidence level are encircled.

Table Captions

Table 1: Description of the 36 Coupled Model Inter-comparison Project phase 5 (CMIP5) models used in our analysis. We use the historical climate experiments from 36 Coupled General Circulation Models (CGCMs) contributing to CMIP5 (Taylor et al. 2012; see url: http://pcmdi9.llnl.gov). The 20-year mean during 1980-1999 in historical simulations defines the present-day climatology. All the diagnostics are performed only for the boreal summer season (June to September, JJAS hereafter).

Table 2: Summary of the coupled ocean-atmosphere experiments performed with the CFSv2 and SINTEX-F2 coupled models. Differences between the coupled simulation configurations are given in the "Setup" column. The first 10 and 5 years of the simulations for SINTEX and CFS, respectively, have been excluded from the analyses presented in this study.

Table 3: TOA net radiation biases (W/m^2) during boreal summer for the globe and the two hemispheres in CFS and SINTEX experiments (see **Table 2**) against radiation fluxes estimates computed from the Clouds and Earth's Radiant Energy System (CERES) system (Kato et al. 2013) over the 2000-2014 period.

Table 4: **(a)** Root-Mean-Square-Error (mm/day) for boreal summer rainfall in the different experiments (see **Table 2**) and different domains against monthly-accumulated precipitation from the Global Precipitation Climatology Project (Huffman et al. 2009) over the 1979-2010 period. **(b)** Spatial correlation for boreal summer rainfall in the different experiments (see **Table 2**) and different domains against monthly-accumulated precipitation from the Global Precipitation Climatology Project (Huffman et al. 2009) over the 1979-2010 period.

Table 5: **(a)** Root-Mean-Square-Error (W/m^2) for boreal summer TOA net radiation, net shortwave radiation and Outgoing Longwave Radiation (OLR) in the different experiments (see **Table 2**) for the whole globe against radiation fluxes estimates computed from the Clouds and Earth's Radiant Energy System (CERES) system (Kato et al. 2013) over the 2000-2014 period. **(b)** Spatial correlation for boreal summer TOA net radiation, net shortwave radiation and OLR in the different experiments (see **Table 2**) for the whole globe against radiation fluxes estimates computed from the Clouds and Earth's Radiant Energy System (CERES) system (Kato et al. 2013) over the 2000-2014 period.

Figure 1

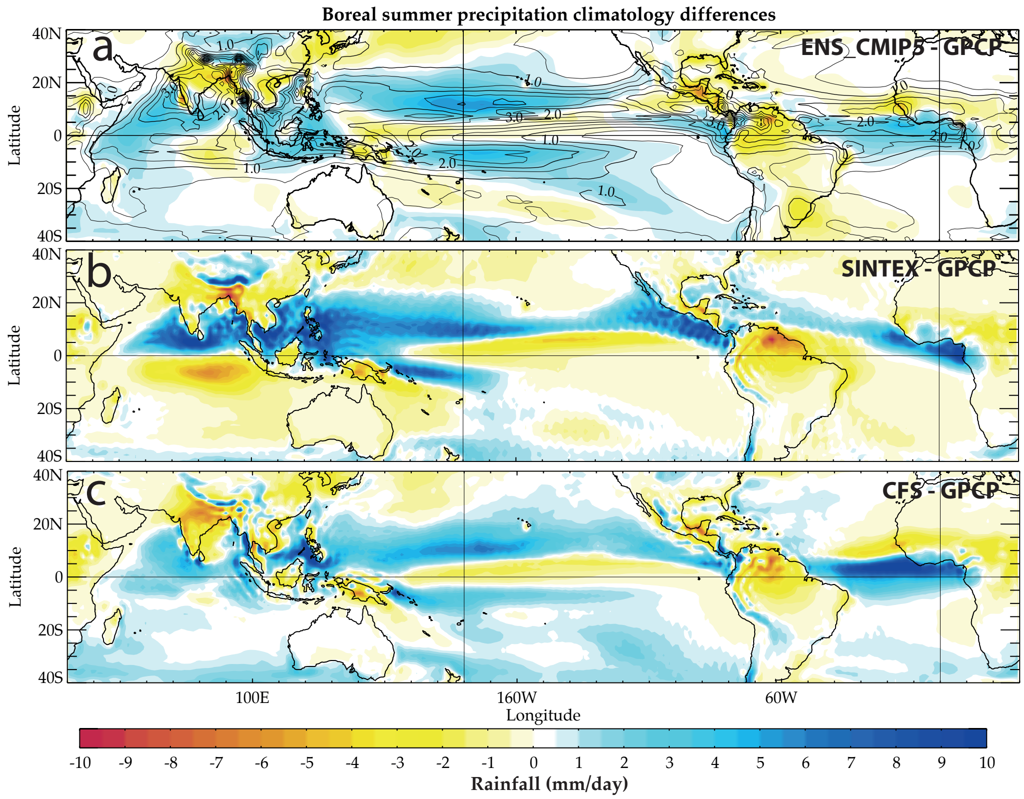

Figure 1: Rainfall biases (mm/day, shading) during boreal summer (e.g. from June to September) in **(a)** ensemble-mean from 36 CMIP5 CGCMs (see **Table 1**), **(b)** SINTEX-F2 coupled model (Masson et al. 2012) and **(c)** Climate Forecast System version2 (CFS) coupled model (Saha et al. 2014) against monthly-accumulated precipitation from the Global Precipitation Climatology Project (Huffman et al. 2009) over the 1979-2010 period. The boreal summer rainfall standard deviation in the 36 CMIP5 CGCMs is also shown as contours (interval every 0.5 mm/day) in panel **(a)**.

Figure 2

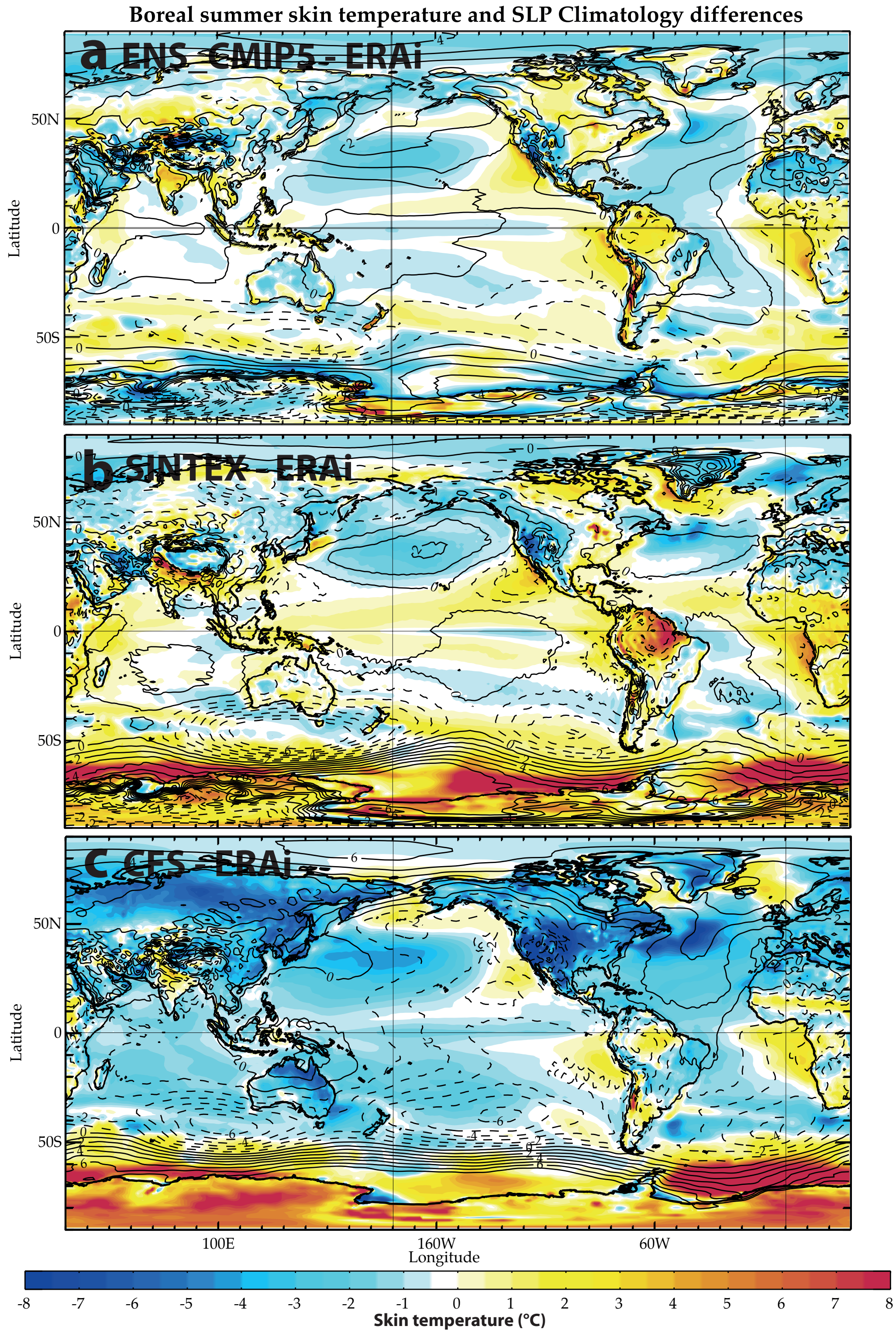

Figure 2: Skin temperature (°C, shading) and SLP (hPa, contours every 1-hPa) biases during boreal summer (e.g. from June to September) in **(a)** ensemble-mean from 36 CMIP5 CGCMs (see **Table 1**), **(b)** SINTEX coupled model and **(c)** CFS coupled model against ERA-Interim reanalysis estimates (Dee et al. 2011) over the 1979-2014 period.

Figure 3

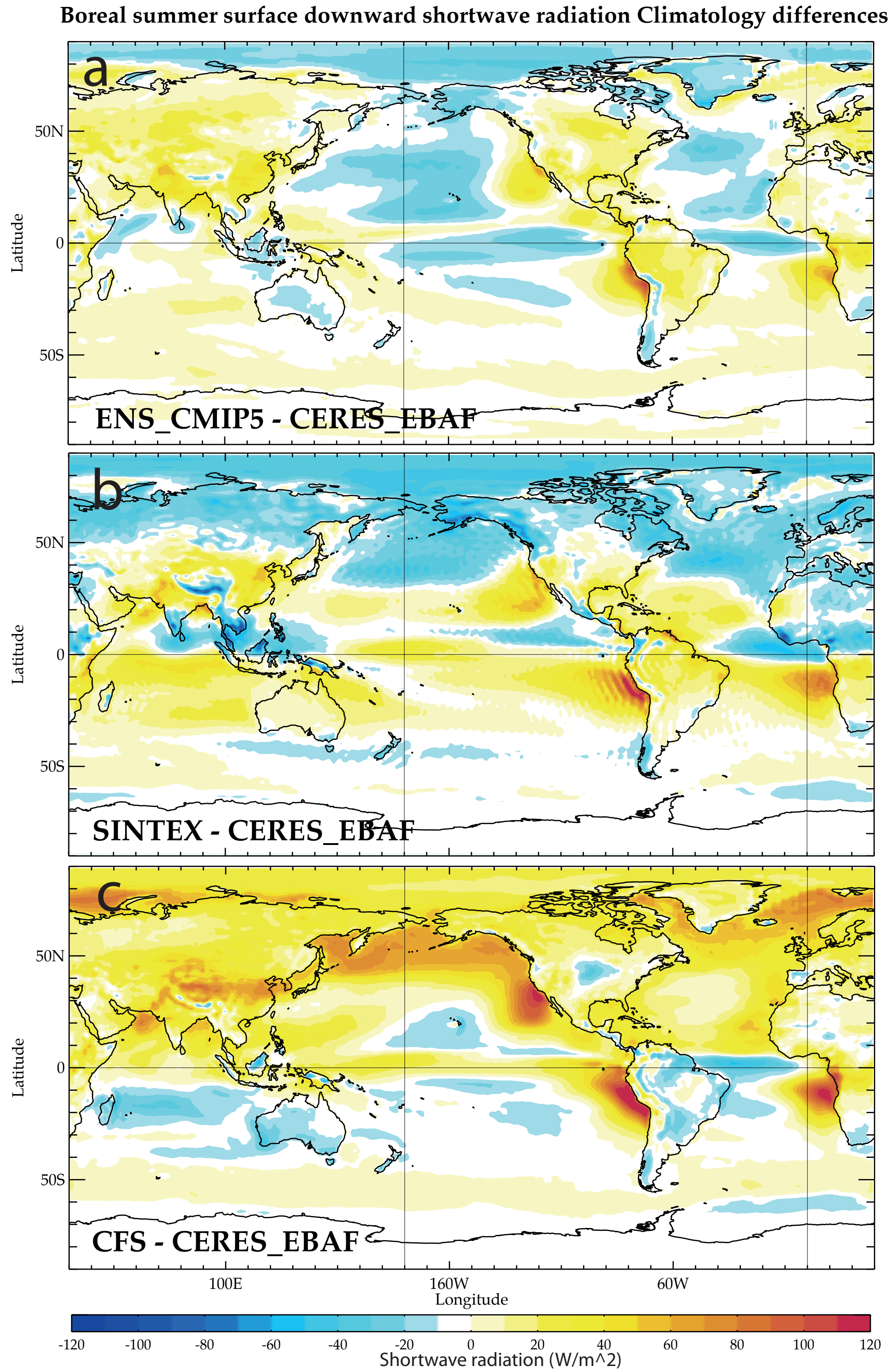

Figure 3: Surface downward shortwave radiation biases (W/m^2) during boreal summer (e.g. from June to September) in **(a)** ensemble-mean from 36 CMIP5 CGCMs (see **Table 1**), **(b)** SINTEX and **(c)** CFS coupled models against estimates from the CERES-EBAF version 2.8 dataset (Kato et al. 2013). The CERES_EBAF boreal summer climatology is estimated from the period 2000-2014.

Figure 4

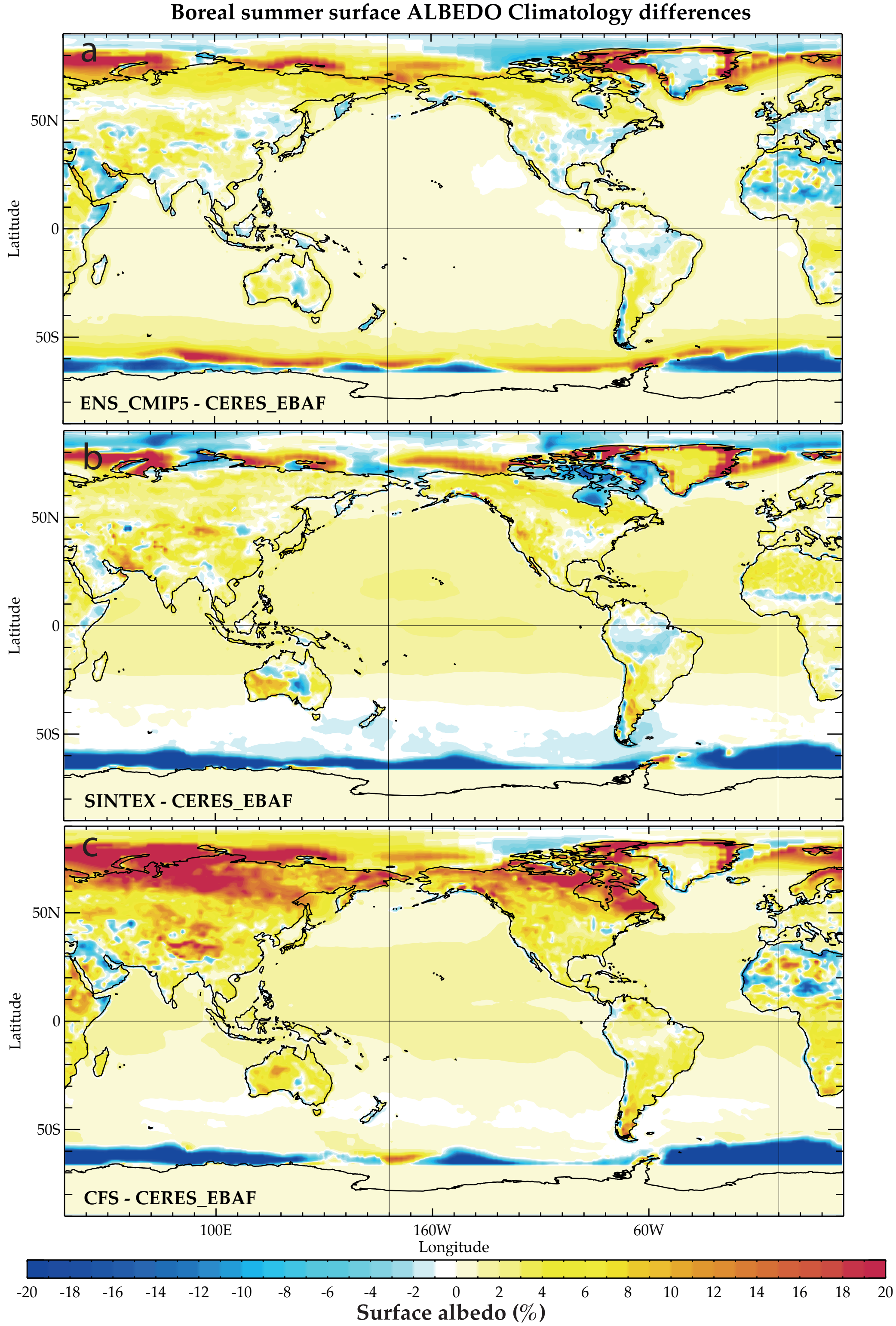

Figure 4: Surface albedo biases (%) during boreal summer (e.g. from June to September) in **(a)** ensemble-mean from 36 CMIP5 CGCMs (see **Table 1**), **(b)** SINTEX coupled model and **(c)** CFS coupled model against radiative fluxes estimates computed from the Clouds and Earth's Radiant Energy System (CERES) system (Kato et al. 2013) over the 2000-2014 period.

Figure 5

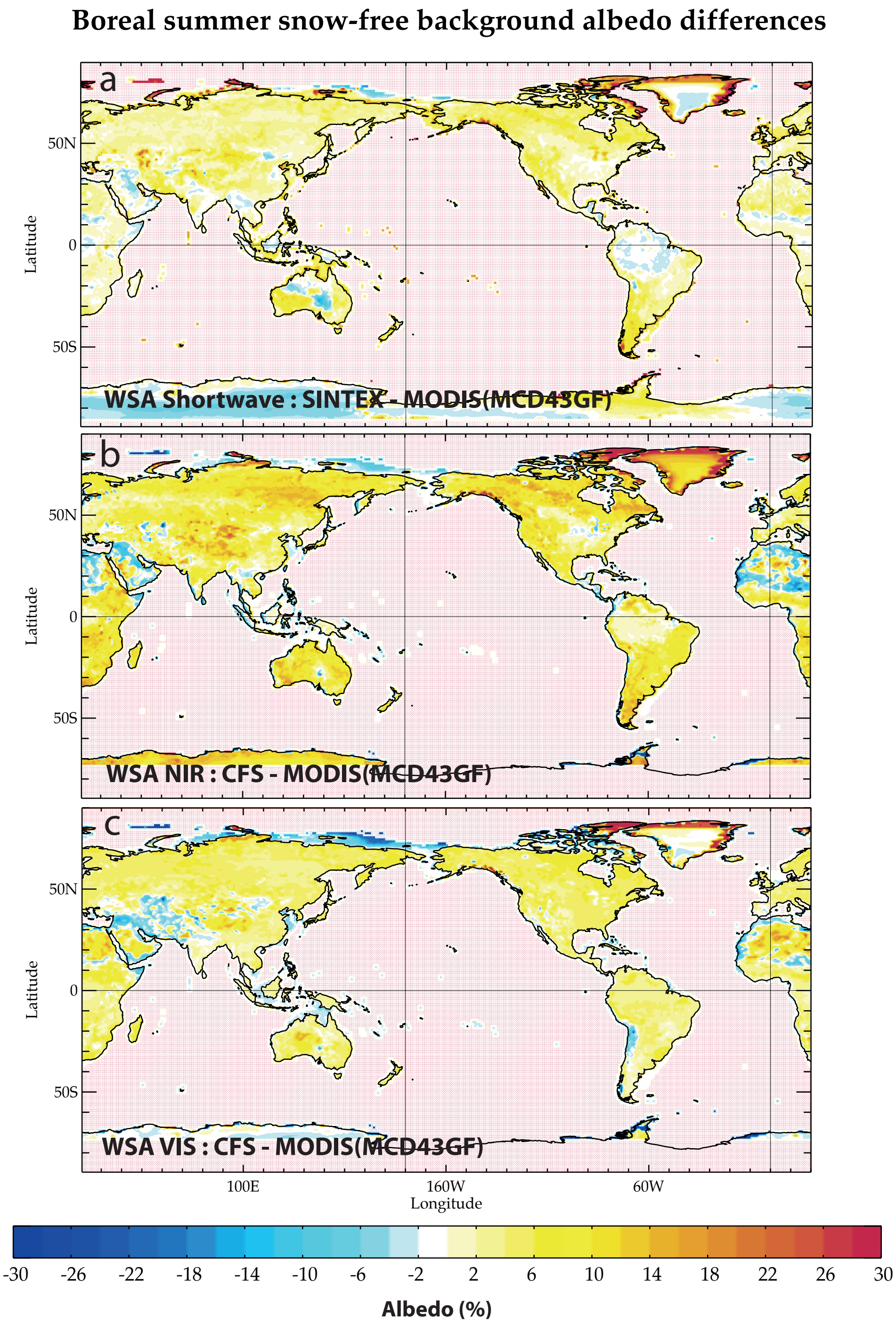

Figure 5: Background snow-free albedo biases (%) over land during boreal summer (e.g. from June to September) for **(a)** diffuse broadband Short-Wave (SW, 0.3–5.0 μm) albedo in SINTEX CGCM, **(b)** diffuse Near-Infra-Red (NIR, >0.7 μm) albedo in CFS CGCM and **(c)** diffuse Visible (VIS, <0.7 μm) albedo in CFS CGCM against corresponding estimates from the Moderate Resolution Imaging Spectro-radiometer (MODIS) snow-free gap-filled white-sky (diffuse) albedo product MCD43GF-v5 (Schaaf et al. 2011). The MODIS climatologies are estimated from the 2003-2013 period. See Section 2 for further details.

Figure 6

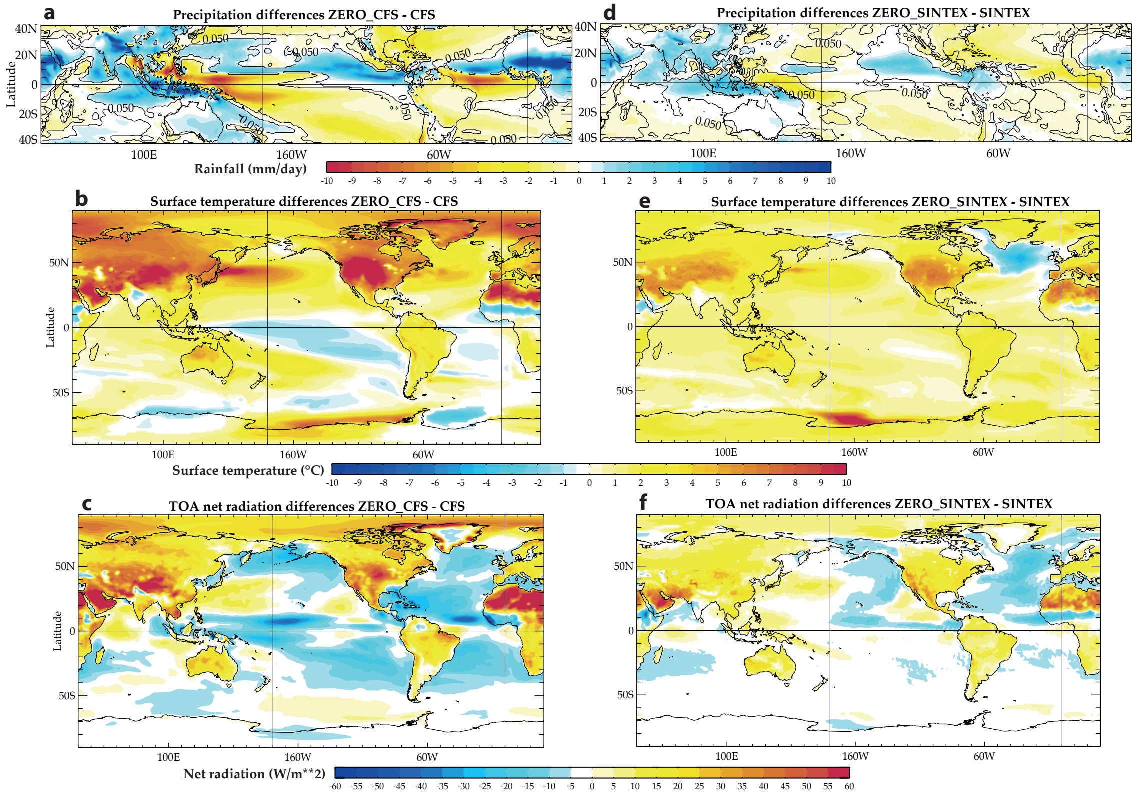

Figure 6: Boreal summer (e.g. from June to September) differences between the ZERO and control experiments (see **Table 2**) for CFS (**a**,**b**,**c**) and SINTEX (**d**,**e**,**f**) models. For **(a,d)** precipitation (mm/day), **(b,e)** surface skin temperature (°C) and **(c,f)** Top Of Atmosphere (TOA) net shortwave radiation (W/m^2). In panels (**a**) and (**b**), differences that are above the 95% confidence level according to a permutation procedure with 9999 shuffles are encircled. In the other panels, the maps only show differences, which are above the 95% confidence level.

Figure 7

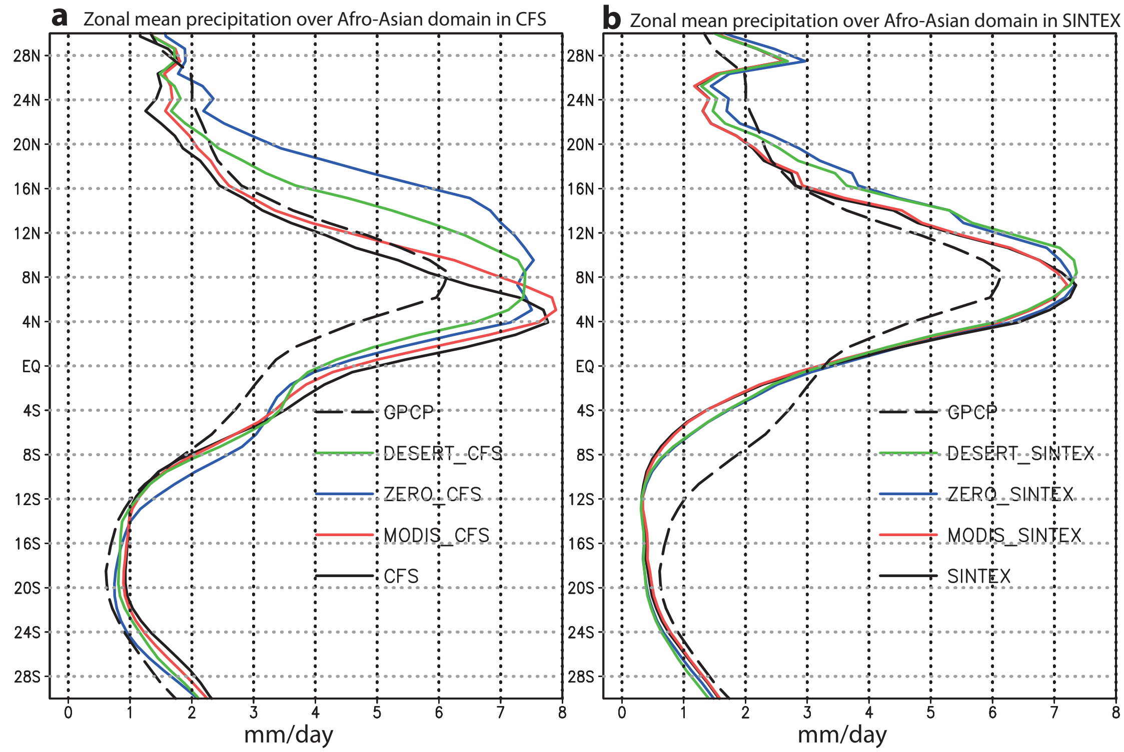

Figure 7: **(a)** Boreal summer (e.g. from June to September) zonal mean precipitation (mm/day) over an African-Asian domain (70°W-100°E) in the different CFS simulations (see **Table 2**) against monthly-accumulated precipitation from the Global Precipitation Climatology Project (Huffman et al. 2009) over the 1979-2010 period, **(b)** as in panel **(a)**, but for the SINTEX simulations (see **Table 2**).

Figure 8

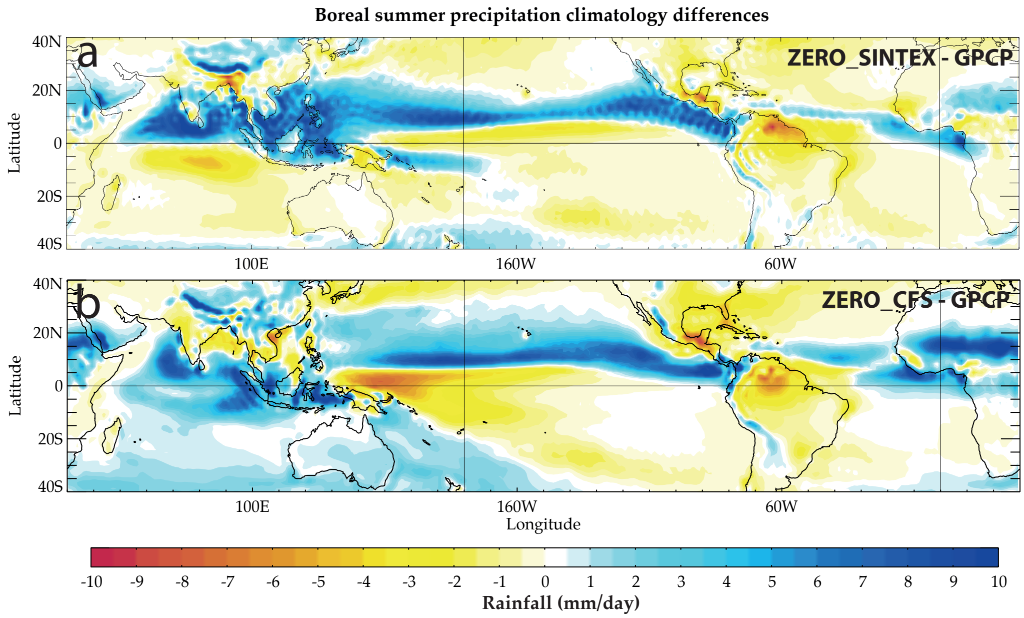

Figure 8: Rainfall biases (mm/day) during boreal summer (e.g. from June to September) in **(a)** ZERO_SINTEX experiment (see **Table 2**) and **(b)** ZERO_CFS experiment (see **Table 2**) against monthly-accumulated precipitation from the Global Precipitation Climatology Project (Huffman et al. 2009) over the 1979-2010 period.

Figure 9

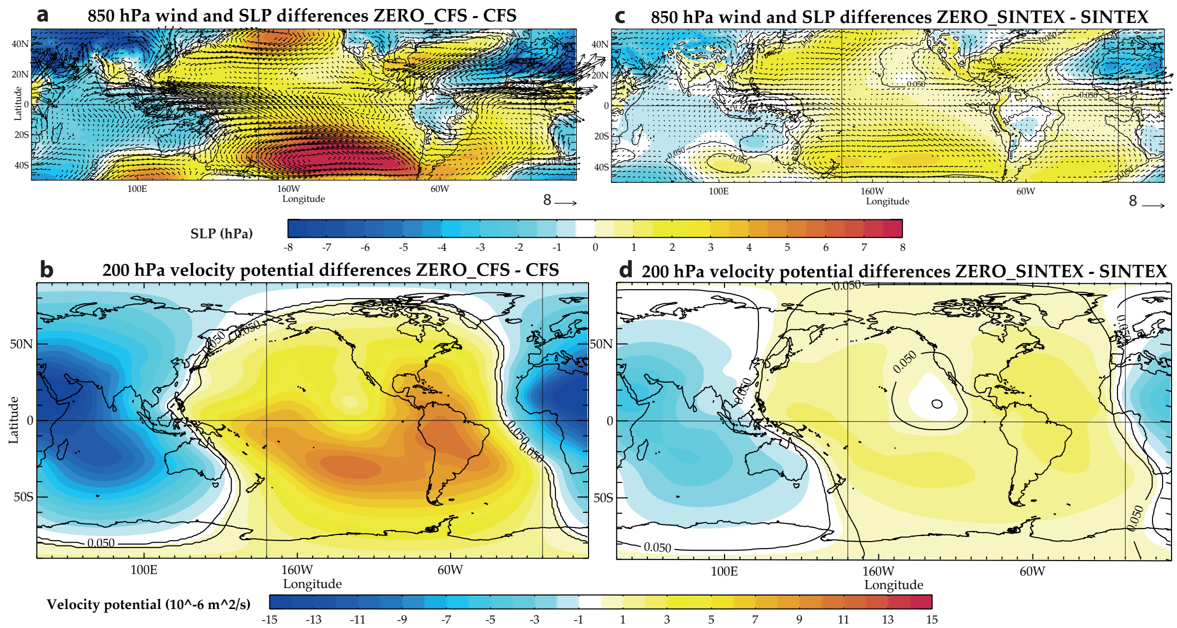

Figure 9: Boreal summer (e.g. from June to September) differences between the ZERO and control experiments (see **Table 2**) for CFS **(a,b)** and SINTEX **(c,d)** models. For **(a,c)** 850-hPa winds (m/s) and Sea Level Pressure (hPa) and **(b,d)** 200-hPa velocity potential (10^{-6} m^2/s). SLP and 200-hPa velocity potential differences, which are above the 95% confidence level according to a permutation procedure with 9999 shuffles are encircled. In panels (**a**) and (**c**), the maps only show the 850-hPa wind differences, which are above the 95% confidence level.

Figure 10

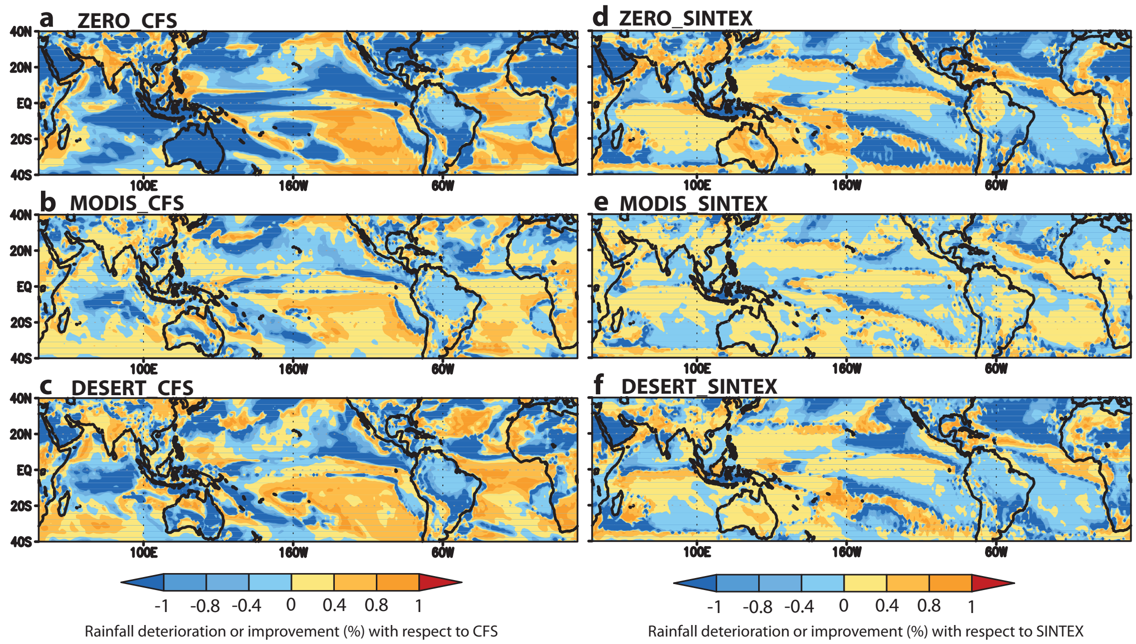

Figure 10: Improvement or deterioration of simulated tropical rainfall during boreal summer in the different experiments (e.g. ZERO, MODIS, DESERT) compared to the biases in the control simulation for each model (e.g. CFS and SINTEX). Following Haywood et al. (2016), for each model, the improvement/deterioration for ZERO, MODIS and DESERT experiments with respect to the control simulation is computed as 1 – abs((EXP-GPCP)/(CTL-GPCP)), where EXP is either ZERO, MODIS or DESERT, GPCP is the boreal summer rainfall climatology for the 1979-2010 period and CTL is the corresponding control simulation. In this way, positive values represent the percentage improvement in boreal summer rainfall (and are bounded by 1) and negative values represent the degradation in boreal summer rainfall compared to the control simulation. **(a)** Boreal summer rainfall improvement or degradation in ZERO_CFS with respect to CFS, **(b)** Boreal summer rainfall improvement or degradation in MODIS_CFS with respect to CFS and **(c)** Boreal summer rainfall improvement or degradation in DESERT_CFS with respect to CFS. **(d)**, **(e)** and **(f)** as **(a)**, **(b)** and **(c)**, respectively, but for SINTEX model.

Figure 11

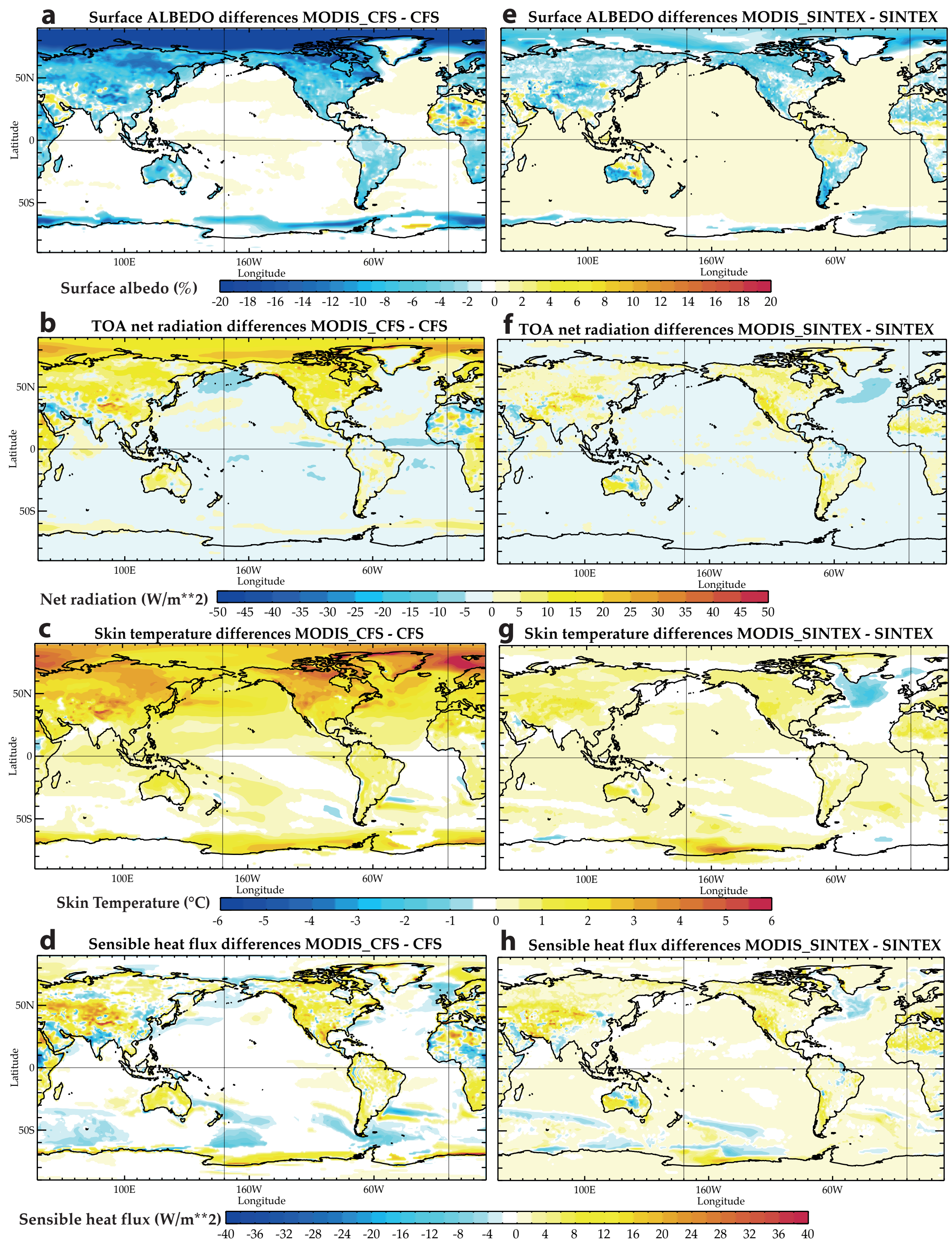

Figure 11: Boreal summer (e.g. from June to September) differences between the MODIS and control experiments (see **Table 2**) for CFS **(a,b,c,d)** and SINTEX **(e,f,g,h)** models. For **(a,e)** albedo (%), **(b,f)** Top Of Atmosphere (TOA) net shortwave radiation (W/m^2), **(c,g)** skin temperature (°C) and **(d,h)** sensible heat flux (W/m^2). The maps only show differences, which are above the 95% confidence level according to a permutation procedure with 9999 shuffles.

Figure 12

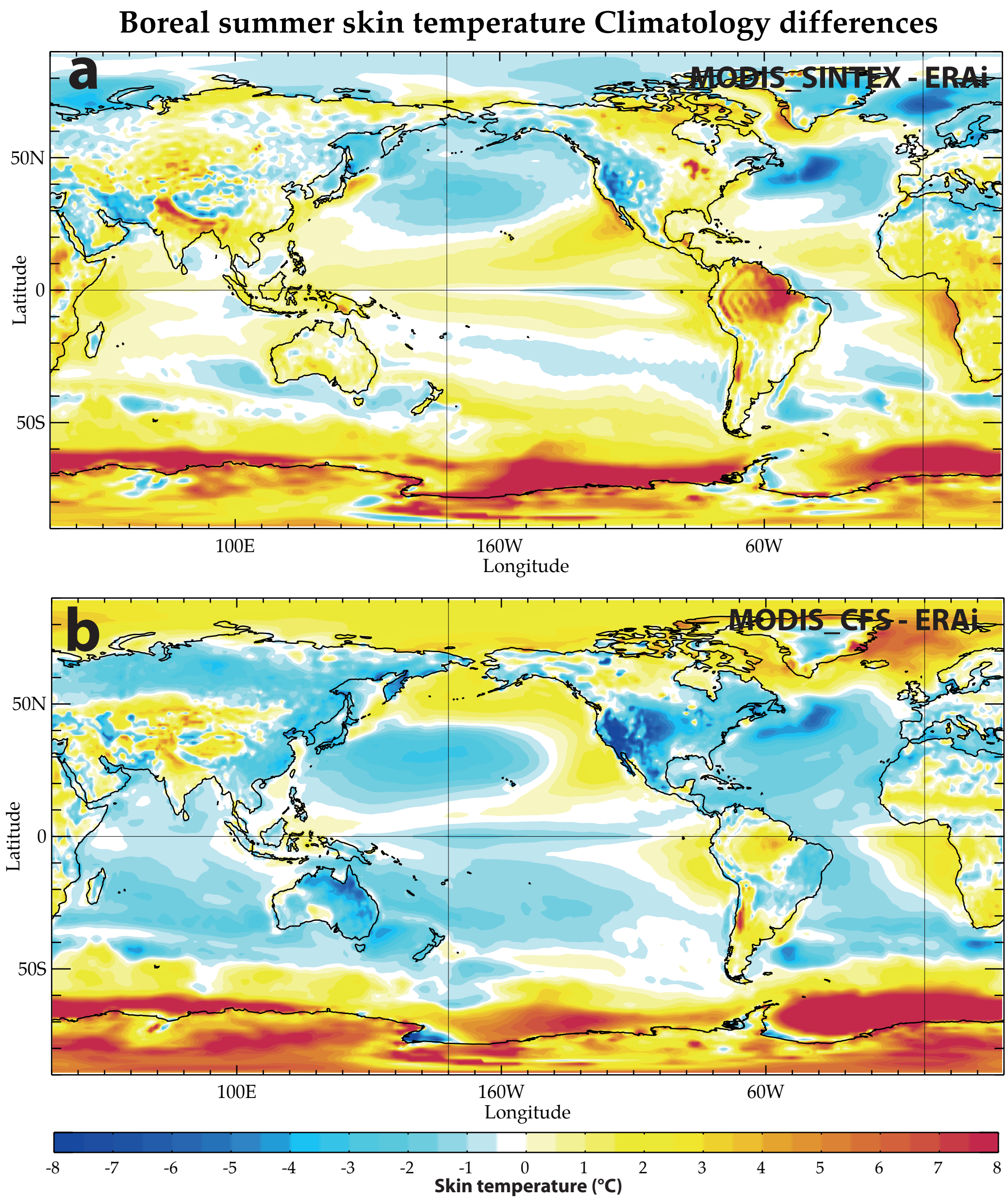

Figure 12: Surface temperature biases (°C) during boreal summer (e.g. from June to September) in **(a)** MODIS_SINTEX experiment (see **Table 2**) and **(b)** MODIS_CFS experiment (see **Table 2**) against ERA-Interim reanalysis climatology (Dee et al. 2011) over the 1979-2014 period.

Figure 13

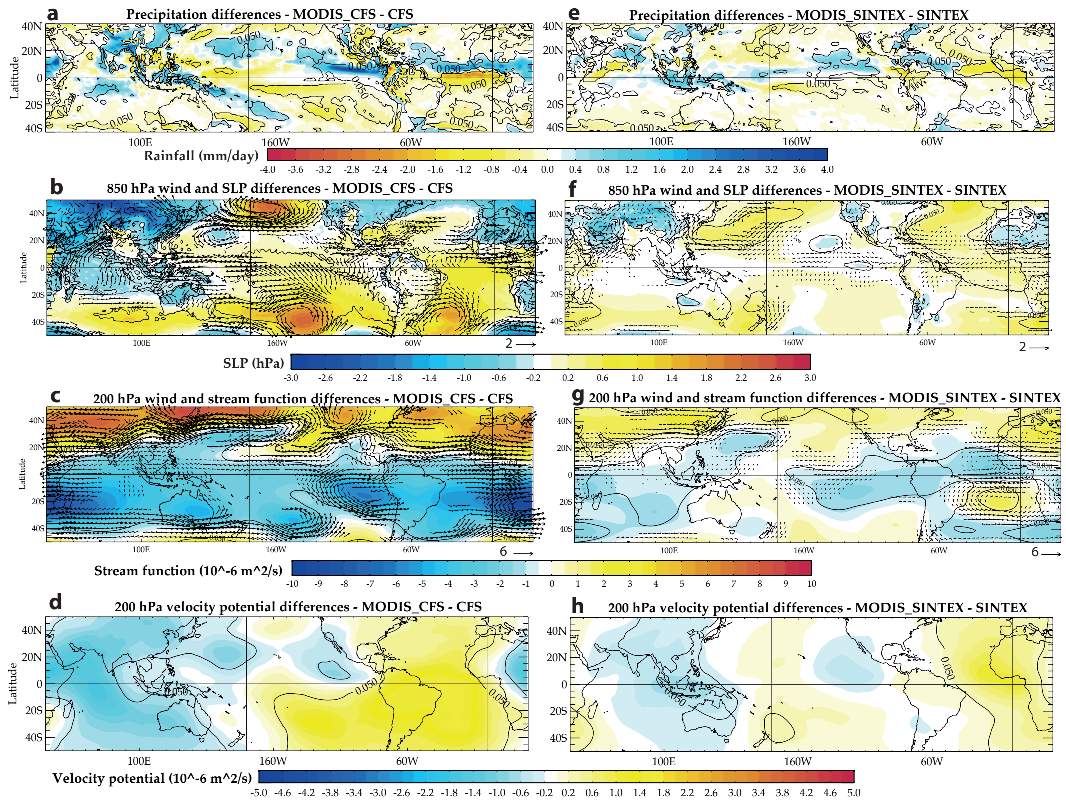

Figure 13: Boreal summer (e.g. from June to September) differences between the MODIS and control experiments (see **Table 2**) for CFS **(a,b,c,d)** and SINTEX **(e,f,g,h)** models. For **(a,e)** precipitation (mm/day), **(b,f)** 850-hPa winds (m/s) and SLP (hPa), **(c,g)** 200-hPa winds (m/s) and 200-hPa stream function (10^{-6} m^2/s) and **(d,h)** 200-hPa velocity potential (10^{-6} m^2/s). In panels **(c)** and **(g)**, positive (negative) values of the stream function denote clockwise (anticlockwise) motions. Precipitation, SLP, 200-hPa stream function and 200-hPa velocity potential differences, which are above the 95% confidence level according to a permutation procedure with 9999 shuffles are encircled. In panels (**b**), (**c**), (**e**) and (**f**), the maps only show the 850 and 200-hPa wind differences, which are above the 95% confidence level.

Figure 14

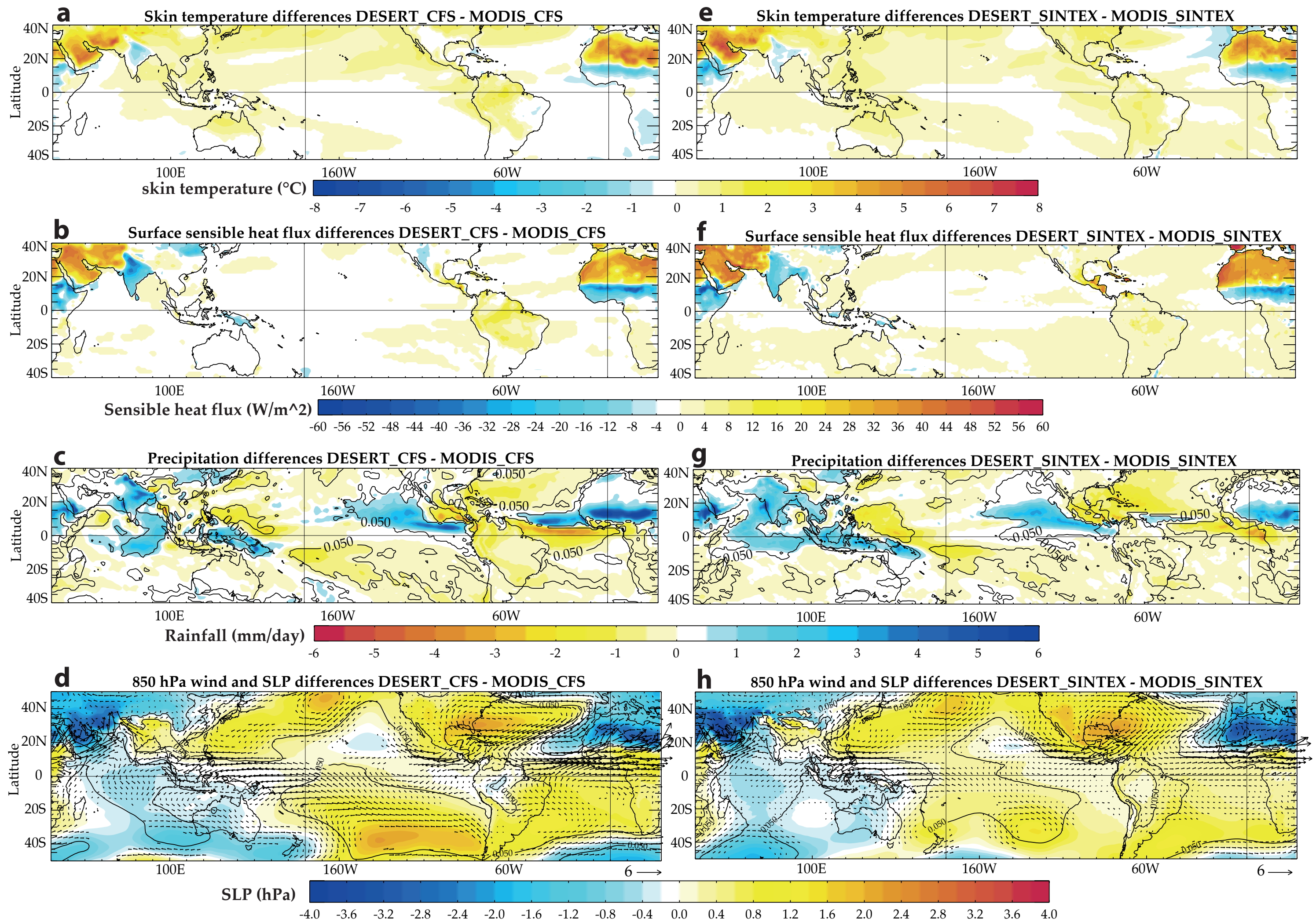

Figure 14: Boreal summer (e.g. from June to September) differences between the DESERT and MODIS experiments (see **Table 2**) for CFS **(a,b,c,d)** and SINTEX **(e,f,g,h)** models. For **(a,e)** skin temperature (°C), **(b,f)** sensible heat flux (W/m^2), **(c,g)** precipitation (mm/day) and **(d,h)** 850-hPa winds (m/s) and Sea Level Pressure (hPa). In panels (**a**), (**b**), (**e**) and (**f**), the maps only show differences, which are above the 95% confidence level according to a permutation procedure with 9999 shuffles. In panels (**c**), (**d**), (**g**) and (**h**), precipitation and SLP differences, which are above the 95% confidence level are encircled and 850-hPa wind differences are shown only if they are above the 95% confidence level.

Figure 15

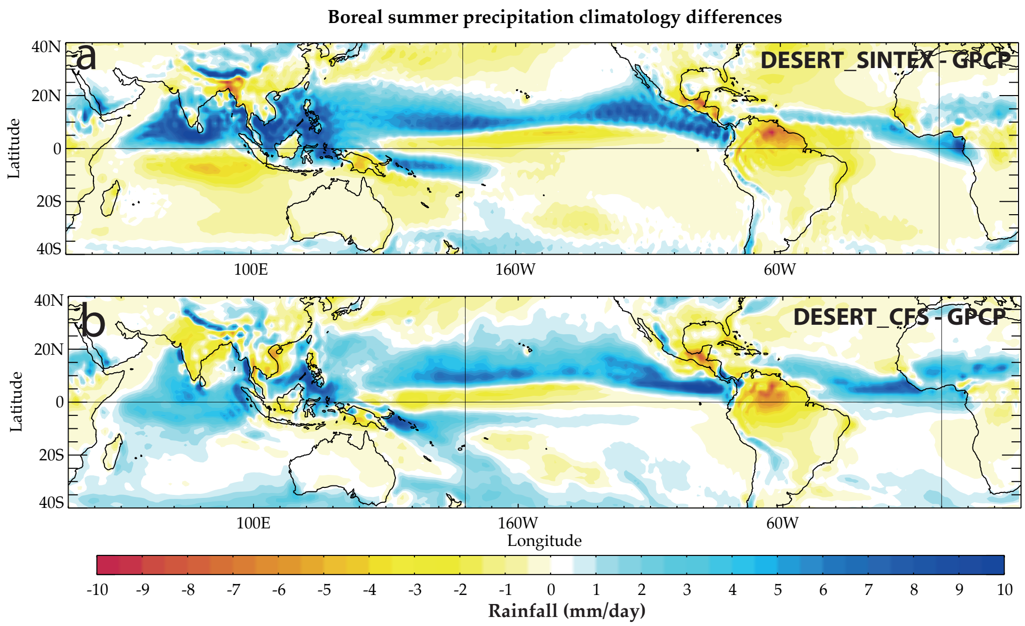

Figure 15: Rainfall biases (mm/day) during boreal summer (e.g. from June to September) in **(a)** DESERT_SINTEX experiment (see **Table 2**) and **(b)** DESERT_CFS experiment (see **Table 2**) against monthly-accumulated precipitation from the Global Precipitation Climatology Project (Huffman et al. 2009) over the 1979-2010 period.

Figure 16

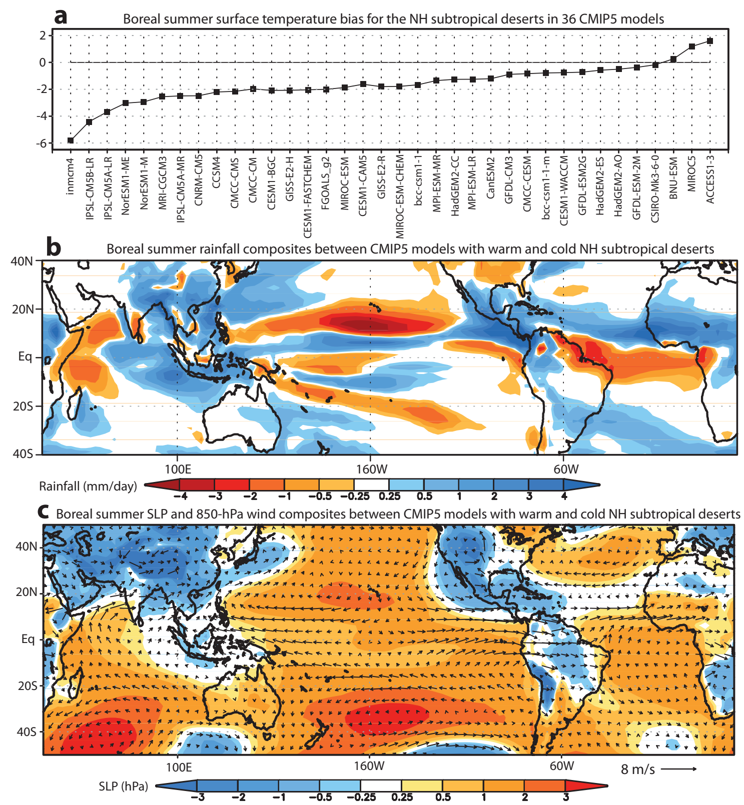

Figure 16: (a) Surface temperature bias (°C) during boreal summer over the same domain (land only: latitude 15°-40°N, longitude 20°W-75°E) as used in the DESERT experiments for 36 CMIP5 models with respect to surface temperature climatology estimated from ERA-Interim reanalysis (Dee et al. 2011) over the 1979-2014 period, **(b)** Rainfall (mm/day) composite differences between the six warmest and six coldest CMIP5 models over the NH subtropical deserts, and **(c),** same as (**b**), but for SLP (hPa) and 850-hPa winds (m/s) composite differences. The six CMIP5 models with the highest (lowest) boreal summer land surface temperature over the NH subtropical deserts (15°-40°N, 20°W-75°E) correspond, respectively, to the CMIP5 models on the extreme right and left of the plot displayed in panel **(a)**.

Figure 17

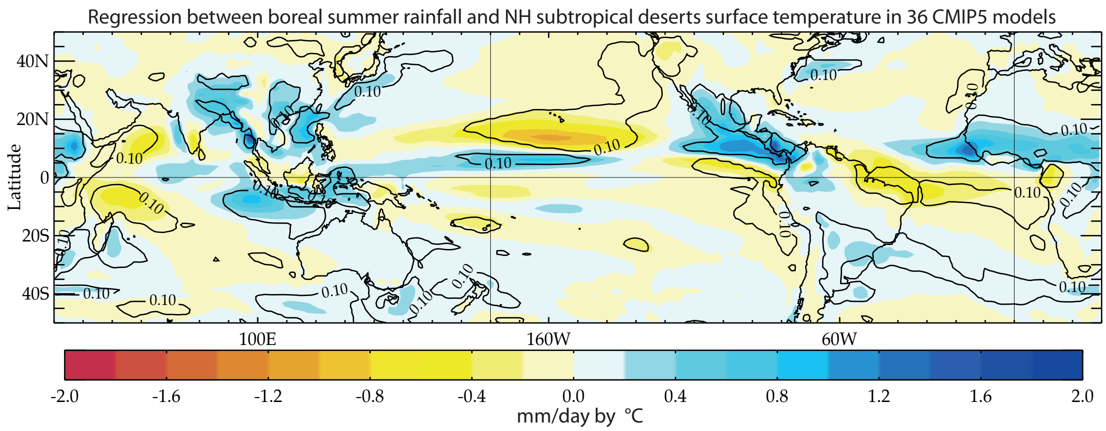

Figure 17: linear regression between rainfall (mm/day) and the surface temperature (°C) over the NH subtropical desert (15°-40°N, 20°W-75°E) in 36 CMIP5 models**.** Regression coefficients significant at the 90% confidence level are encircled.

No.	Couple model name	Institution	Atmospheric resolution (Lon×Lat, Levels)
1	ACCESS 1.3	Commonwealth Scientific and Industrial Research Organisation and Bureau of Meteorology Australia	192×145, 38
2	BCC-CSM1.1	Beijing Climate Center, China Meteorological Administration	128×64, 26
3	BCC-CSM1.1.m	Beijing Climate Center, China Meteorological Administration	320x160, 26
4	BNU-ESM	Beijing Normal University	128x64, 26
5	CanESM2	Canadian Centre for Climate Modeling and Analysis	128×64 , 35
6	CCSM4	National Center for Atmospheric Research	288×192, 26
7	CESM1-BGC	Community Earth System Model Contributors	288×192, 26
8	CESM1-CAM5	Community Earth System Model Contributors	288×192, 26
9	CESM1FASTCHEM	Community Earth System Model Contributors	288×192, 26
10	CESM1-WACCM	Community Earth System Model Contributors	144×96, 66
11	CMCC-CESM	Centro Euro-Mediterraneo sui Cambiamenti Climatici	96x48, 39
12	CMCC-CM	Centro Euro-Mediterraneo sui Cambiamenti Climatici	480x240, 31
13	CMCC-CMS	Centro Euro-Mediterraneo sui Cambiamenti Climatici	192x96, 95
14	CNRM-CM5	Centre National de Recherches Meteorologiques	256x128, 31
15	CSIRO-Mk3.6.0	Commonwealth Scientific and Industrial Research Organisation	192×96, 18
16	FGOALS-g2	Institute of Atmospheric Physics, Chinese Academy of Sciences	128x60, 26
17	GFDL-CM3	Geophysical Fluid Dynamics Laboratory	144×90, 48
18	GFDL-ESM-2G	Geophysical Fluid Dynamics Laboratory	144×90, 48
19	GFDL-ESM-2M	Geophysical Fluid Dynamics Laboratory	144×90, 48
20	GISS-E2-H	NASA Goddard Institute for Space Studies	144×90, 40
21	GISS-E2-R	NASA Goddard Institute for Space Studies	144×90, 40
22	HadGEM2-AO	Met Office Hadley Center, UK	192x145, 38
23	HadGEM2-CC	Met Office Hadley Center, UK	192x145, 60
24	HadGEM2-ES	Met Office Hadley Center, UK	192x145, 38
25	INM-CM4	Institute for Numerical Mathematics	180×120, 21
26	IPSL-CM5A-LR	Institut Pierre-Simon Laplace	96×96, 39
27	IPSL-CM5A-MR	Institut Pierre-Simon Laplace	144×143, 39
28	IPSL-CM5B-LR	Institut Pierre-Simon Laplace	96×96, 39
29	MIROC5	Atmosphere and Ocean Research Institute (The University of Tokyo), and National Institute for Environmental Studies, Japan Agency for Marine-Earth Science and Technology	256x128, 40
30	MIROC-ESM	Japan Agency for Marine-Earth Science and Technology, Atmosphere and Ocean Research Institute (The University of Tokyo), and National Institute for Environmental Studies	128×64, 80
31	MIROC-ESM-CHEM	Japan Agency for Marine-Earth Science and Technology, Atmosphere and Ocean Research Institute (The University of Tokyo), and National Institute for Environmental Studies	128×64, 80
32	MPI-ESM-LR	Max Planck Institute for Meteorology (MPI-M)	192x96, 47
33	MPI-ESM-MR	Max Planck Institute for Meteorology (MPI-M)	192x96, 95
34	MRI-CGCM3	Meteorological Research Institute, Japan	320x160, 48
35	NorESM1-M	Norwegian Climate Centre	144×96, 26
36	NorESM1-ME	Norwegian Climate Centre	144×96, 26

Table 1: Description of the 36 Coupled Model Inter-comparison Project phase 5 (CMIP5) models used in our analysis. We use the historical climate experiments from these 36 Coupled General Circulation Models (CGCMs) contributing to CMIP5 (Taylor et al. 2012; see url: http://pcmdi9.llnl.gov). The 20-year mean during 1980-1999 in historical simulations defines the present-day climatology. All the diagnostics are performed only for the boreal summer season (June to September, JJAS hereafter).

Table 2

Acronym	Coupled model	Duration (years)	Setup
SINTEX	SINTEX-F2	210	Control experiment
ZERO_SINTEX	SINTEX-F2	60	Background snow-free broadband shortwave albedo set to zero over land
MODIS_SINTEX	SINTEX-F2	110	Prescribed background snow-free broadband shortwave albedo replaced by MODIS estimates
DESERT_SINTEX	SINTEX-F2	60	Prescribed background snow-free broadband shortwave albedo replaced by MODIS estimates and further decrease by -0.2 over the Sahara, Arabia and Middle-East deserts (land domain: latitude 15°-40°N, longitude 20°W-75°E)
CFS	CFSv2	80	Control experiment
ZERO_CFS	CFSv2	30	Background snow-free diffuse visible and near-infra-red albedo set to zero over land
MODIS_CFS	CFSv2	60	Prescribed background snow-free diffuse visible and near-infra-red albedo replaced by MODIS estimates
DESERT_CFS	CFSv2	30	Prescribed background snow-free diffuse visible and near-infra-red albedo replaced by MODIS estimates and further decrease by -0.2 over the Sahara, Arabia and Middle-East deserts (land domain: latitude 15°-40°N, longitude 20°W-75°E)

Table 2: Summary of the coupled ocean-atmosphere experiments performed with the CFSv2 and SINTEX-F2 coupled models. Differences between the coupled simulation configurations are given in the "Setup" column.

Table 3

Domain	**CFS bias**	**SINTEX bias**
Globe	4.6	0.3
NH	8.5	-0.7
SH	0.8	1.2

Table 3: TOA net radiation biases (W/m^2) during boreal summer for the globe and the two hemispheres in CFS and SINTEX experiments (see **Table 2**) against radiation fluxes estimates computed from the Clouds and Earth's Radiant Energy System (CERES) system (Kato et al. 2013) over the 2000-2014 period.

Table 4

Simulation/domain	**Tropics** (30°S-30°N)	**Africa** (10°S-20°N, 60°W-40°E)	**South Asia** (0-25°N, 50°E-100°E)
CFS	2.2	3.2	3.3
ZERO_CFS	2.8	3.5	3.6
MODIS_CFS	2.1	2.3	3.0
DESERT_CFS	2.2	2.3	3.0
SINTEX	2.6	2.4	4.4
ZERO_SINTEX	2.7	1.97	4.8
MODIS_SINTEX	2.5	2	4.2
DESERT_SINTEX	2.5	2.0	4.7

(a) Root-Mean-Square-Error (mm/day) for boreal summer rainfall in the different experiments (see **Table 2**) and different domains against monthly-accumulated precipitation from the Global Precipitation Climatology Project (Huffman et al. 2009) over the 1979-2010 period.

Simulation/domain	**Tropics** (30°S-30°N)	**Africa** (10°S-20°N, 60°W-40°E)	**South Asia** (0-25°N, 50°E-100°E)
CFS	0.83	0.61	0.76
ZERO_CFS	0.76	0.67	0.74
MODIS_CFS	0.86	0.77	0.79
DESERT_CFS	0.86	0.87	0.84
SINTEX	0.82	0.77	0.67
ZERO_SINTEX	0.83	0.80	0.71
MODIS_SINTEX	0.84	0.81	0.7
DESERT_SINTEX	0.84	0.82	0.8

(b) Spatial correlation for boreal summer rainfall in the different experiments (see **Table 2**) and different domains against monthly-accumulated precipitation from the Global Precipitation Climatology Project (Huffman et al. 2009) over the 1979-2010 period.

Table 5

Simulation/variable	**TOA net radiation**	**TOA net shortwave radiation**	**OLR**
CFS	18.5	18.2	10.6
ZERO_CFS	25	25.1	14.2
MODIS_CFS	18.5	18.6	9.3
DESERT_CFS	21.1	20.1	10.1
SINTEX	13.3	16.1	10.1
ZERO_SINTEX	15.9	17.8	10.1
MODIS_SINTEX	13.5	15.9	9.7
DESERT_SINTEX	17.6	18.4	10.8

(a) Root-Mean-Square-Error (W/m^2) for boreal summer TOA net radiation, net shortwave radiation and Outgoing Longwave Radiation (OLR) in the different experiments (see **Table 2**) for the whole globe against radiation fluxes estimates computed from the Clouds and Earth's Radiant Energy System (CERES) system (Kato et al. 2013) over the 2000-2014 period.

Simulation/variable	**TOA net radiation**	**TOA net shortwave radiation**	**OLR**
CFS	0.97	0.98	0.95
ZERO_CFS	0.95	0.97	0.91
MODIS_CFS	0.98	0.98	0.97
DESERT_CFS	0.97	0.98	0.96
SINTEX	0.98	0.98	0.96
ZERO_SINTEX	0.98	0.98	0.96
MODIS_SINTEX	0.98	0.99	0.96
DESERT_SINTEX	0.97	0.98	0.95

(b) Spatial correlation for boreal summer TOA net radiation, net shortwave radiation and OLR in the different experiments (see **Table 2**) for the whole globe against radiation fluxes estimates computed from the Clouds and Earth's Radiant Energy System (CERES) system (Kato et al. 2013) over the 2000-2014 period.